NTHMP Landslide Benchmark Results for NHWAVE, Version 3.0

BY

Cheng Zhang[1], James T. Kirby[1],

Stephan Grilli[2], Gangfeng Ma[3],

Fengyan Shi[1], and Michael Shelby[2]

[1] Center for Applied Coastal Research, Department of Civil and Environmental Engineering, University of Delaware, Newark, DE 19716

[2] Department of Ocean Engineering, University of Rhode Island, Narragansett, RI 02882

[3] Department of Civil and Environmental Engineering, Old Dominion University, Norfolk, VA 23529

RESEARCH REPORT NO. CACR-17-05
DECEMBER 2017

CENTER FOR APPLIED COASTAL RESEARCH

University of Delaware
Newark, Delaware 19716

Abstract

We describe the application of NHWAVE model to the study of seven benchmark problems established for the NTHMP Landslide Tsunami Model Benchmarking Workshop, held in January 2017 at Galveston, Texas. Model performance is seen to be good, with the model being used in a range of configurations including solid, viscous fluid, and granular slide motions.

Contents

List of Figures

List of Tables

1 Introduction

NHWAVE is a non-hydrostatic wave-resolving model initially developed by Ma et al. (2012) to simulate the propagation of fully dispersive, fully nonlinear surface waves and resulting circulation in complex 3D coastal environments. The model is formulated in time-dependent, surface and terrain-following σ-coordinates, and can provide instantaneous descriptions of surface displacement and the three dimensional velocity and pressure fields. Wave breaking is handled naturally by the shock-capturing properties of the model's finite volume TVD formulation. NHWAVE has been extended to incorporate various landslide models in order to simulate tsunami wave generation by solid slides (Ma et al., 2012), multiphase simulation of suspended sediment load (Ma et al., 2013), granular debris flows (Ma et al., 2015) and viscous fluid slides (Kirby et al., 2016).

In this report, we provide an overview of the model equations and numerical approach in Section 2. The landslide benchmarks (obtained from http://www1.udel.edu/kirby/landslide/problems.html) are then described in Section 3, with conclusions following in Section 4.

2 Model description

This section describes the basic model and extensions to cover the simulation of submarine landslide motions.

2.1 NHWAVE model equations

The governing equations of NHWAVE are the incompressible Navier-Stokes equations in well-balanced conservative form, formulated in time-dependent surface and terrain-following σ coordinate, which is defined as

$$t = t^* \quad x = x^* \quad y = y^* \quad \sigma = \frac{z^* + h}{D} \tag{1}$$

where the total water depth $D(x, y, t) = h(x, y, t) + \eta(x, y, t)$, $h(x, y, t)$ is the water depth with respect to the datum, which is temporally varying with landslides, $\eta(x, y, t)$ is the free surface elevation.

With σ coordinate transformation, the well-balanced mass and momentum equations are given by

$$\frac{\partial D}{\partial t} + \frac{\partial Du}{\partial x} + \frac{\partial Dv}{\partial y} + \frac{\partial \omega}{\partial \sigma} = 0 \tag{2}$$

$$\frac{\partial \mathbf{U}}{\partial t} + \frac{\partial \mathbf{F}}{\partial x} + \frac{\partial \mathbf{G}}{\partial y} + \frac{\partial \mathbf{H}}{\partial \sigma} = \mathbf{S}_h + \mathbf{S}_p \tag{3}$$

where $\mathbf{U} = (Du, Dv, Dw)^T$ and ω is the vertical velocity in the σ coordinate image domain. The

fluxes are given by

$$\mathbf{F} = \begin{pmatrix} Duu + \frac{1}{2}g\eta^2 + gh\eta \\ Duv \\ Duw \end{pmatrix} \quad \mathbf{G} = \begin{pmatrix} Duv \\ Dvv + \frac{1}{2}g\eta^2 + gh\eta \\ Dvw \end{pmatrix} \quad \mathbf{H} = \begin{pmatrix} u\omega \\ v\omega \\ w\omega \end{pmatrix}$$

The source terms on the right hand side of equation (3) account for the contributions from hydro-static pressure and non-hydrostatic pressure respectively, written as

$$\mathbf{S}_h = \begin{pmatrix} g\eta\frac{\partial h}{\partial x} \\ g\eta\frac{\partial h}{\partial y} \\ 0 \end{pmatrix} \quad \mathbf{S}_p = \begin{pmatrix} -\frac{D}{\rho}(\frac{\partial p}{\partial x} + \frac{\partial p}{\partial \sigma}\frac{\partial \sigma}{\partial x^*}) \\ -\frac{D}{\rho}(\frac{\partial p}{\partial y} + \frac{\partial p}{\partial \sigma}\frac{\partial \sigma}{\partial y^*}) \\ -\frac{1}{\rho}\frac{\partial p}{\partial \sigma} \end{pmatrix}$$

where p is the dynamic pressure.

To solve the water depth D, we integrate the continuity equation (2) from $\sigma = 0$ to 1. By using the boundary conditions at the bottom and surface for ω, we may obtain the equation for free surface movement.

$$\frac{\partial D}{\partial t} + \frac{\partial}{\partial x}(D \int_0^1 ud\sigma) + \frac{\partial}{\partial y}(D \int_0^1 vd\sigma) = 0 \tag{4}$$

2.2 Simulating slides as suspended sediment load

In this approach, landslides are simulated as water-sediment mixture, which can be diffused and diluted during their movement. The dense plume is driven by the baroclinic pressure forcing, which is introduced by the spatial density variation. The suspended sediment concentration can be computed from the convection-diffusion equation for suspended sediment load, which is given as follows in σ coordinate.

$$\begin{aligned} \frac{\partial DC}{\partial t} + \frac{\partial DuC}{\partial x} + \frac{\partial DvC}{\partial y} + \frac{\partial(\omega - w_s)C}{\partial \sigma} &= \frac{\partial}{\partial x}[D(\nu + \frac{\nu_t}{\sigma_h})\frac{\partial C}{\partial x}] \\ &+ \frac{\partial}{\partial y}[D(\nu + \frac{\nu_t}{\sigma_h})\frac{\partial C}{\partial y}] + \frac{1}{D}\frac{\partial}{\partial \sigma}[(\nu + \frac{\nu_t}{\sigma_v})\frac{\partial C}{\partial \sigma}] \end{aligned} \tag{5}$$

where C is the concentration of suspended sediment and w_s is sediment settling velocity. In the following, we will vary the sediment settling velocity to study its effects on landslide motion and associated tsunami waves. σ_h and σ_v are horizontal and vertical Schmidt numbers for sediment, respectively.

To solve the above equation, boundary conditions are needed to be specified at all the physical boundaries. Specifically, at the free surface, the vertical sediment flux is zero. At the bed-fluid interface, there is mass exchange of suspended sediment, which accounts for sediment erosion and deposition. However, in the following studies of submarine landslide, we assume that the submarine landslide is a self-sustained system. Thus, no mass exchange occurs at the bed. Therefore, a

2

zero vertical flux boundary condition is imposed at both free surface and bottom.

$$(\nu + \frac{\nu_t}{\sigma_v})\frac{1}{D}\frac{\partial C}{\partial \sigma} + w_s C = 0 \tag{6}$$

2.3 Simulating slides as a discrete lower layer: Viscous slide equations

In this approach, landslides are simulated using a water layer (consisting of the basic NHWAVE model) overlying a depth-integrated slide layer). The slide layer here consists of a single depth-integrated model based on the equations for a highly viscous Neutonian fluid, following the work of Fine et al. (1998), and using a standard horizontal Cartesian coordinate system (x, y) referenced to the level still water surface and coinciding with the coordinate system used in NHWAVE. The sketch of this two-way coupled model is presented in Figure 1. The upper layer is freshwater with density ρ_f, surface elevation $\eta(x, y, t)$ and water depth h from still water to slide surface, while the lower layer is sediments with density ρ_s, dynamic viscosity μ_s, velocity $(u(x, y, t), v(x, y, t), w(x, y, t))$ and thickness of layer $D(x, y, t)$. Since the slide is bounded by its upper surface $z = -h(x, y, t)$ and the seabed surface $z = -h_s(x, y, t)$, the slide thickness $D(x, y, t) = h_s(x, y, t) - h(x, y, t)$. The long-wave regime, viscous regime and mild-slope assumption give the horizontal velocity profile

$$u(x, y, z, t) = \frac{3}{2}U(x, y, t)(2\xi - \xi^2) \tag{7}$$

$$v(x, y, z, t) = \frac{3}{2}V(x, y, t)(2\xi - \xi^2) \tag{8}$$

where U and V are depth-averaged horizontal velocity, and $\xi = \frac{z+h_s}{D}$ and represents seabed when $\xi = 0$ and slide surface when $\xi = 1$.

The resulting depth-averaged governing equations for the slide are given in conservative form by

$$\frac{\partial \mathbf{E}}{\partial t} + \frac{\partial \mathbf{F}}{\partial x} + \frac{\partial \mathbf{G}}{\partial y} = \mathbf{S}_p + \mathbf{S}_h + \mathbf{S}_\tau + \mathbf{S}_f \tag{9}$$

where $\mathbf{E} = (D, DU, DV)^T$, and the fluxes are

$$\mathbf{F} = \begin{pmatrix} DU \\ \frac{6}{5}DUU + \frac{1}{2}gD^2 \\ \frac{6}{5}DUV \end{pmatrix} \qquad \mathbf{G} = \begin{pmatrix} DV \\ \frac{6}{5}DVU \\ \frac{6}{5}DVV + \frac{1}{2}gD^2 \end{pmatrix}$$

The source terms are given by

$$\mathbf{S}_h = \begin{pmatrix} 0 \\ -\frac{D}{\rho_s}\frac{\partial p_f}{\partial x} \\ -\frac{D}{\rho_s}\frac{\partial p_f}{\partial y} \end{pmatrix} \qquad \mathbf{S}_p = \begin{pmatrix} 0 \\ gD\frac{\partial h_s}{\partial x} \\ gD\frac{\partial h_s}{\partial y} \end{pmatrix}$$

3
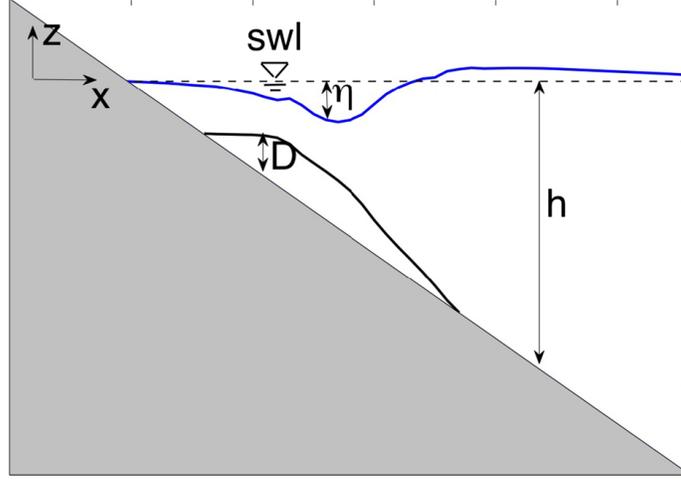
Figure 1: Definition sketch for underwater landslide. (From Grilli et al., 2016)

$$
\mathbf{S}_\tau = \begin{pmatrix} 0 \\ \nu_s \left[D \left(\frac{\partial^2 U}{\partial x^2} + \frac{\partial^2 U}{\partial y^2} \right) - 3\frac{U}{D} \right] \\ \nu_s \left[D \left(\frac{\partial^2 V}{\partial x^2} + \frac{\partial^2 V}{\partial y^2} \right) - 3\frac{V}{D} \right] \end{pmatrix} \quad \mathbf{S}_f = \begin{pmatrix} 0 \\ \frac{gn^2}{D^{1/3}} \sqrt{U^2 + V^2} U \\ \frac{gn^2}{D^{1/3}} \sqrt{U^2 + V^2} V \end{pmatrix}
$$

where $\nu_s = \mu_s/\rho_s$ is kinematic viscosity of slide and n is Manning friction coefficient.

2.4   Simulating slides as a discrete lower layer: Granular slide equations

A version of the depth-integrated lower slide layer has been developed by Ma et al. (2015), based on the granular flow model of Iverson and Denlinger (2001). This version of the model has been developed in slope-oriented coordinates and is formulated only for a planar slope. Use of the model thus requires a mapping from slope-oriented coordinates to horizontal coordinates in order to locate slide properties properly in the NHWAVE grid. The governing equations for the granular slide are given by

$$
\frac{\partial \mathbf{U}}{\partial t} + \frac{\partial \mathbf{F}}{\partial x'} + \frac{\partial \mathbf{G}}{\partial y'} = \mathbf{S} \tag{10}
$$

in which (x', y') are slope-oriented coordinates, and $\mathbf{U} = (h_a, h_a u_a, h_a v_a)^T$. The fluxes are given by

$$
\mathbf{F} = \begin{pmatrix} h_a u_a \\ h_a u_a^2 + \frac{1}{2}[(1-\lambda)k_{act/pass} + \lambda]g_{z'}h_a^2 \\ h_a u_a v_a \end{pmatrix} \tag{11}
$$

4

$$\mathbf{G} = \begin{pmatrix} h_a v_a \\ h_a u_a v_a \\ h_a v_a^2 + \frac{1}{2}[(1-\lambda)k_{act/pass} + \lambda]g_{z'}h_a^2 \end{pmatrix} \tag{12}$$

The source term is

$$\mathbf{S} = \begin{pmatrix} 0 \\ S_{x'} \\ S_{y'} \end{pmatrix} \tag{13}$$

where

$$\begin{aligned}
S_{x'} =\, & g_{x'}h_a - \frac{h_a}{\rho}\frac{\partial P_h^f}{\partial x'} - (1-\lambda)g_{z'}h_a \tan\phi_{bed}\frac{u_a}{\sqrt{u_a^2 + v_a^2}} \\
& - sgn\left(S_{x'y'}\right)h_a\frac{\partial}{\partial y'}[g_{z'}h_a(1-\lambda)]\sin\phi_{int}
\end{aligned} \tag{14}$$

$$\begin{aligned}
S_{y'} =\, & g_{y'}h_a - \frac{h_a}{\rho}\frac{\partial P_h^f}{\partial y} - (1-\lambda)g_{z'}h_a \tan\phi_{bed}\frac{v_a}{\sqrt{u_a^2 + v_a^2}} \\
& - sgn\left(S_{y'x'}\right)h_a\frac{\partial}{\partial x'}[g_{z'}h_a(1-\lambda)]\sin\phi_{int}
\end{aligned} \tag{15}$$

where $g_{z'}$ is the component of gravitational acceleration normal to the slope, $k_{act/pass}$ is the Earth pressure coefficient given by Ma et al. (2015), ϕ_{bed} is the friction angle of the granular material contacting the bed, ϕ_{int} is the internal friction angle of the granular solid, λ is a parameter to be determined.

2.5 Numerical method

The well-balanced continuity and momentum equations (2) and (3) are discretized by a combined finite-volume and finite-difference approach with a second-order Godunov-type scheme. Following the numerical framework of NHWAVE (Ma et al., 2012), the velocities are defined at the cell centers, while the pressure is defined at the vertically-facing cell faces in order to accurately prescribe zero pressure condition at the free surface. The two-stage second-order nonlinear Strong Stability-Preserving (SSP) Runge-Kutta scheme (Gottlieb et al., 2001) is adopted for time stepping in order to obtain second-order temporal accuracy. At the first stage, an intermediate quantity $\mathbf{U}^{(1)}$ is evaluated using a typical first-order, two-step projection method given by

$$\frac{\mathbf{U}^* - \mathbf{U}^n}{\Delta t} = -\left(\frac{\partial \mathbf{F}}{\partial x} + \frac{\partial \mathbf{G}}{\partial y} + \frac{\partial \mathbf{H}}{\partial \sigma}\right)^n + \mathbf{S}_h^n \tag{16}$$

$$\frac{\mathbf{U}^{(1)} - \mathbf{U}^*}{\Delta t} = \mathbf{S}_p^{(1)} \tag{17}$$

where $\mathbf{U}^n$ represents $\mathbf{U}$ value at time level n, $\mathbf{U}^*$ is the intermediate value in the two-step projection method, and $\mathbf{U}^{(1)}$ is the final first stage estimate.

At the second stage, the velocity field is updated to a second intermediate level using the same projection method, after which the Runge-Kutta algorithm is used to obtain a final value of the solution at the $n + 1$ time level.

$$\frac{\mathbf{U}^* - \mathbf{U}^{(1)}}{\Delta t} = -\left(\frac{\partial \mathbf{F}}{\partial x} + \frac{\partial \mathbf{G}}{\partial y} + \frac{\partial \mathbf{H}}{\partial \sigma}\right)^{(1)} + \mathbf{S}_h^{(1)} \tag{18}$$

$$\frac{\mathbf{U}^{(2)} - \mathbf{U}^*}{\Delta t} = \mathbf{S}_p^{(2)} \tag{19}$$

$$\mathbf{U}^{n+1} = \frac{1}{2}\mathbf{U}^n + \frac{1}{2}\mathbf{U}^{(2)} \tag{20}$$

In the projection step (16) - (17) and (14)), a Poisson equation can be derived by applying the continuity equation (Ma et al., 2012). The Poisson equation is discretized by finite difference method, resulting in a linear equation system with a coefficient matrix of 15 diagonal lines. The linear system is solved using the high performance preconditioner HYPRE software library.

3 Landslide benchmarks

In this section, six laboratory cases and one field case are studied as landslide benchmarks, and results of numerical calculations are compared to the data from experiments or field observations. The following benchmark problems are studied in this section:

1. Two-dimensional submarine solid block

2. Three-dimensional submarine solid block

3. Three-dimensional submarine/subaerial triangular solid block

4. Two-dimensional submarine granular slide

5. Two-dimensional subaerial granular slide

6. Three-dimensional subaerial granular slide

7. Field Case: Slide at Port Valdez, AK during 1964 Alaska Earthquake

3.1 Benchmark 1: Two-dimensional submarine solid block

The 2D landslide benchmark is covered here based on one laboratory experiment conducted by Grilli and Watts (2005). In the experiment, the model slide down a plane slope with an angle $\theta = 15$ deg in a wave tank of water depth $h_o = 1.05$ m and width 0.2 m. And the dimensions of slide model are length $B = 1$ m, maximum thickness $T = 0.052$ m, and width $w = 0.2$ m which is same to tank width. The model initial submergence d in this case is 0.259 and the free surface
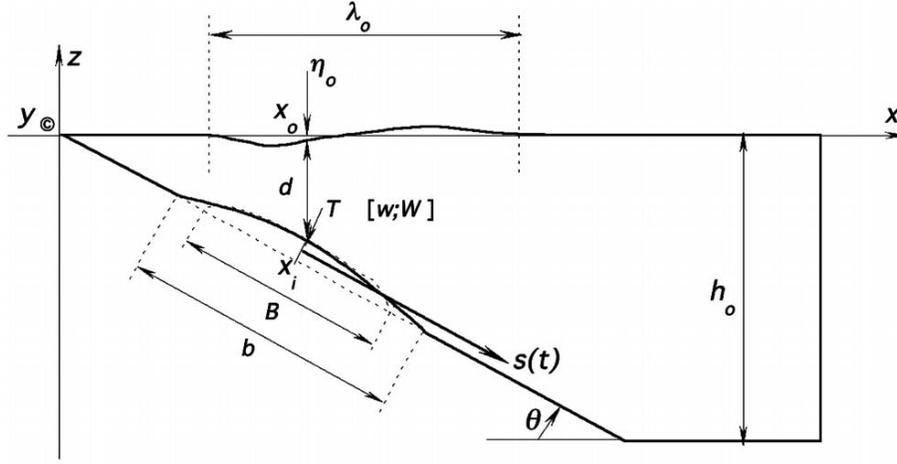
Figure 2: Sketch of main parameters for 2D landslide benchmark. [from Grilli and Watts, 2005].

elevation recorded at 4 locations of $x = 1.234, 1.549, 1.864, 2.179$ m. The experimental setup is shown in Figure 2.

In the simulation, a uniform grid size of 0.02 m is used to discretize the computational domain of 10×0.2 m and the water depth is divided into 3 layers. Here, the solid block is represented by a Gaussian shape defined as

$$\zeta = \frac{T}{1-\varepsilon} \left[\operatorname{sech}^2(k\xi) - \varepsilon \right] \tag{21}$$

where

$$b = \frac{2C}{k} \qquad k = \frac{2C'}{B} \qquad C' = \frac{4\tanh(C - \varepsilon C)}{\pi(1-\varepsilon)} \qquad C = \operatorname{acosh} \frac{1}{\sqrt{\varepsilon}} \tag{22}$$

and $\varepsilon \in]0, 1[$ is spreading parameter. Here ε is chosen as 0.75. According to the theoretical law of motion, the slide move in the way of

$$\frac{s}{s_0} = \log \left\{ \cosh \left(\frac{t}{t_0} \right) \right\} \tag{23}$$

where

$$t_0 = \frac{u_t}{a_0} \qquad s_0 = \frac{u_t^2}{a_0} \tag{24}$$

and in this case, $a_0 = 0.75\,\mathrm{m/s^2}$ and $u_t = 1.258\,\mathrm{m/s}$.

Figure 3 shows the comparison of surface elevation between numerical results from NHWAVE, from BEM results (Grilli and Watts 2005) and experimental data at locations $x = 1.234, 1.549, 1.864$ and 2.179 m.

7
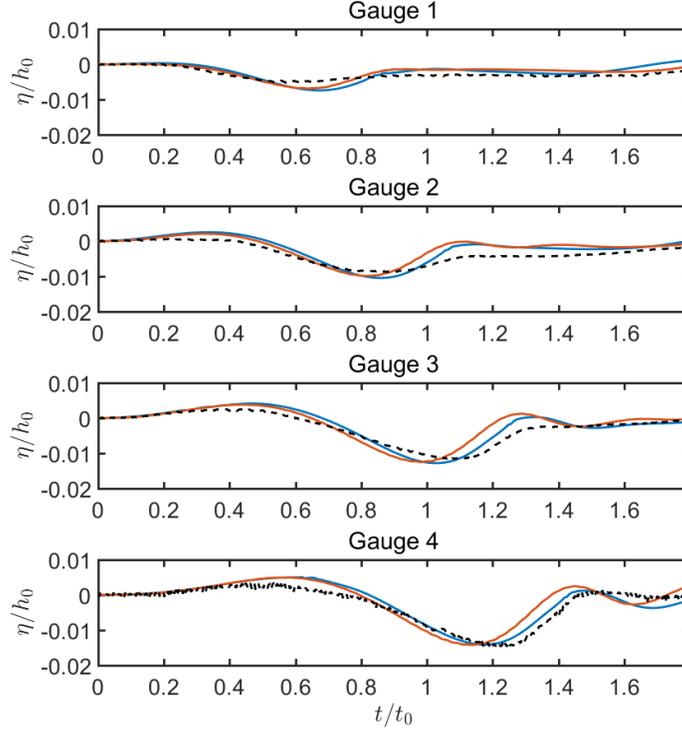
Figure 3: Benchmark 1: Comparison of surface elevations obtained from NHWAVE with solid slide motion, with BEM results (Grilli and Watts 2005) and experimental data at locations of $x = 1.234, 1.549, 1.864, 2.179$ m. Solid blue lines represent NHWAVE results, solid red lines represent BEM results and dashed black lines represent experimental data.

Looking more closely at the modeled surface elevation shows that small defects may develop (Figure 4). This problem may be caused by non-smoothness at two ends of the slide block. Two approaches are used here to eliminate these bumps. The first way is to use smaller ε in specifying the slide geometry in (21), and the second way is represent the block with a Cosine shape defined as

$$\zeta = \frac{T}{2}\left[1 - \cos(2\pi\frac{\xi}{b})\right] \tag{25}$$

Figure 5 shows three options of slide cross-section geometry for 2D model and Figure 6 shows the numerical results of them. It can be seen both ways can smooth the bumps out.

8
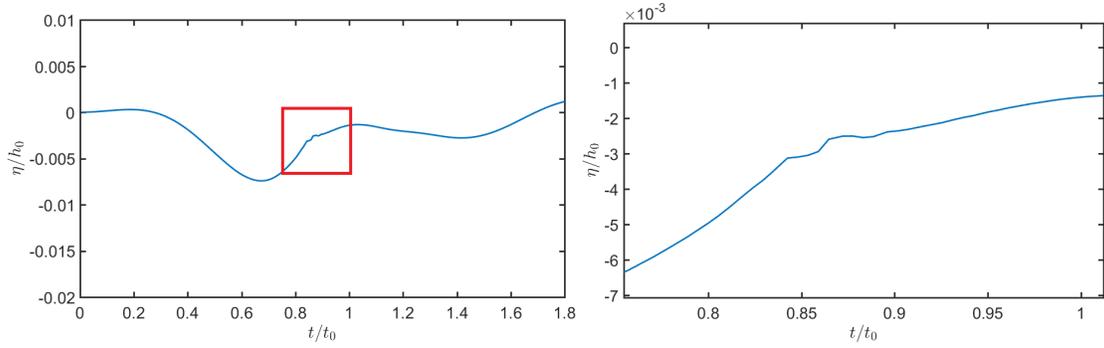
Figure 4: Zoom-in of the surface elevation curve at Gauge 1.
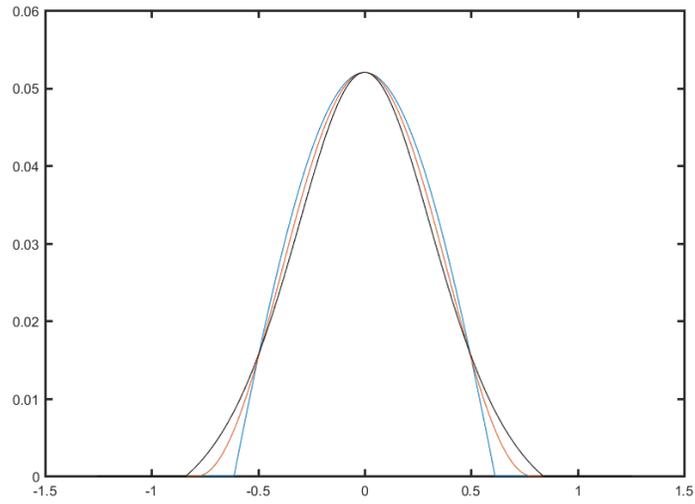
Figure 5: Slide cross-section geometry for 2D model. Blue line represents Gaussian shape with $\varepsilon = 0.75$, black line represents the one with $\varepsilon = 0.1$ and red line represents Cosine shape.

9
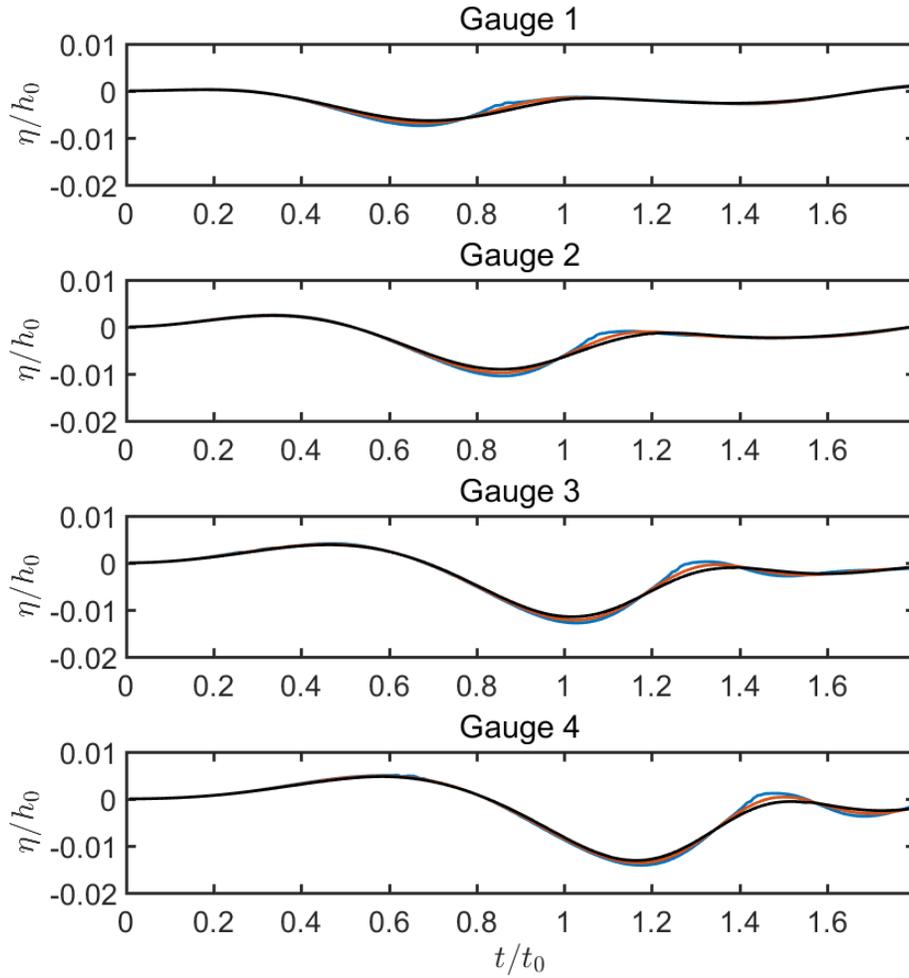
Figure 6: Benchmark 1: Comparison of free surface elevation between the numerical results with three types of model geometry. Blue line represents Gaussian shape with $\varepsilon = 0.75$, black line represents the one with $\varepsilon = 0.1$ and red line represents Cosine shape.

3.2 Benchmark 2: Three-dimensional submarine solid block

For benchmark#2, we applied the model to simulate an series of idealized 3D landslide cases, of which the experiments have been performed by Enet and Grilli (2007). Similar to the 2D case, the model slide down a plane slope with an angle $\theta = 15$ deg in a wave tank of water depth $h_o = 1.5$ m and width 3.7 m. But the solid block now has semielliptical cross sections in x-z both plane and y-z plane and its dimensions are down-slope length $b = 0.395$ m, cross-slope width $w = 0.680$ m, and maximum thickness $T = 0.082$ m. Seven model initial submergence $d = 61, 80, 100, 120, 140, 149$ and 189 m are set for different cases and the surface elevation recorded at 4 locations of (x,y)= $(x_0, 0), (1.469, 350), (1.929, 0), (1.919, 500)$ in meters, where x_0 is the initial location of the slide. The experimental setup is shown in Figure 7.
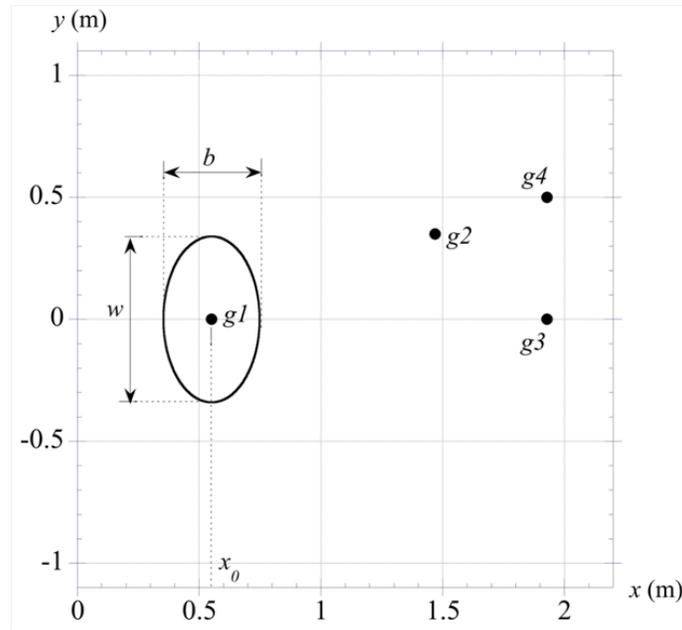
Figure 7: Sketch of main parameters for 3D landslide benchmark.

In the simulation, a uniform grid size of 0.02 m is used to discretize half the mirror-symmetric computational domain of 10×3.6 m and the water depth is divided into 3 layers. Here, the solid block is represented by a Gaussian shape defined as

$$\zeta = \frac{T}{1 - \varepsilon} \left[\operatorname{sech}(k_b \xi) \operatorname{sech}(k_w \eta) - \varepsilon \right] \tag{26}$$

where

$$k_b = \frac{2C}{b} \qquad k_w = \frac{2C}{w} \qquad C = \operatorname{acosh} \frac{1}{\varepsilon} \tag{27}$$

11

d (mm)	61	80	100	120	140	149	189
x_0 (mm)	551	617	696	763	846	877	1017
$a_0(\mathrm{m/s^2})$	1.20	1.21	1.19	1.17	1.14	1.20	1.21
$u_t(\mathrm{m/s})$	1.70	1.64	1.93	2.03	2.13	1.94	1.97

Table 1: Slide motion parameters for the seven cases.

and $\varepsilon \in]0, 1[$ is spreading parameter. Here a identical $\varepsilon = 7.17$ is chosen for all cases. And the 3D benchmark shares the same theoretical law of motion with the 2D case, and all parameters of the motion are listed in Table 1.

Figures 8–14 show the comparison of surface elevation between numerical results of the 7 cases and experimental data at locations of $(x, y) = (x_0, 0), (1.469, 350), (1.929, 0)$ and $(1.919, 500)$m.

In NHWAVE, first order forward difference scheme is used to evaluate the first and second derivative of h in time. To eliminate the differencing error, expressions for the derivatives based on the analytical formula for the bottom shape are given by

$$\frac{\mathrm{d}h}{\mathrm{d}t} = k_b \cos\theta \left(\zeta + \frac{\varepsilon T}{1 - \varepsilon}\right) \frac{\mathrm{d}s}{\mathrm{d}t} \tanh(k_b\xi) \tag{28}$$

$$\frac{\mathrm{d}^2h}{\mathrm{d}t^2} = k_b \cos\theta \left(\zeta + \frac{\varepsilon T}{1 - \varepsilon}\right) \left(\frac{\mathrm{d}^2s}{\mathrm{d}t^2} \tanh(k_b\xi) - k_b \cos\theta \left(\frac{\mathrm{d}s}{\mathrm{d}t}\right)^2 \mathrm{sech}(k_b\xi)^2\right) \tag{29}$$

Figure 15 and 16 show the comparison of results for case $d = 61$ mm and case $d = 120$ mm between numerical solution and analytical solution for $\mathrm{d}h/\mathrm{d}t$ and $\mathrm{d}^2h/\mathrm{d}t^2$. It can be seen that two results are almost overlapped, so the the differencing error of derivatives of h has minor effect on the results.

Another issue we would like to raise is that for all cases in this benchmark, non-hydrostatic pressure has to be considered. Figure 17 and 18 show that the results without considering non-hydrostatic pressure deviate a lot the the results with non-hydrostatic pressure and thus the experimental data.
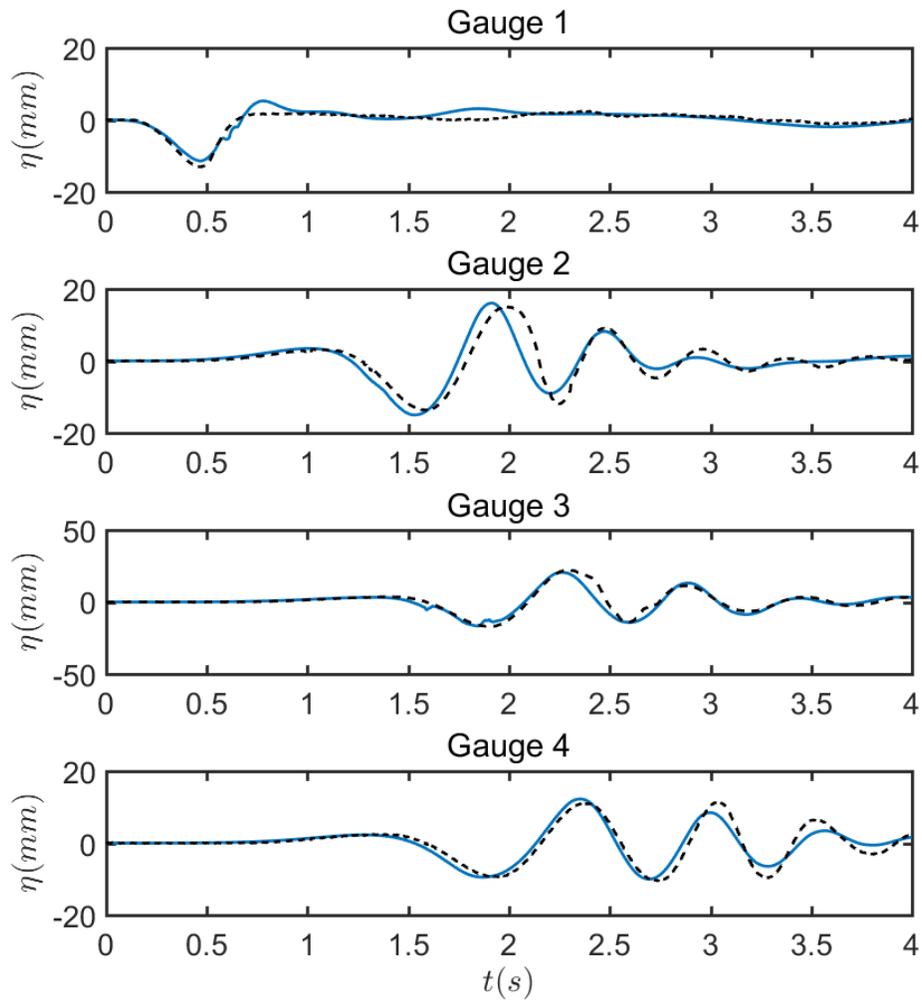
Figure 8: Benchmark 2: Comparison of surface elevation between numerical results of the case $d = 61$ mm from NHWAVE and experimental data at locations of (x,y)= $(0.551, 0)$, $(1.469, 350)$, $(1.929, 0)$, $(1.919, 500)$ in meters. Solid blue lines represent numerical results and dashed black lines represent experimental data.
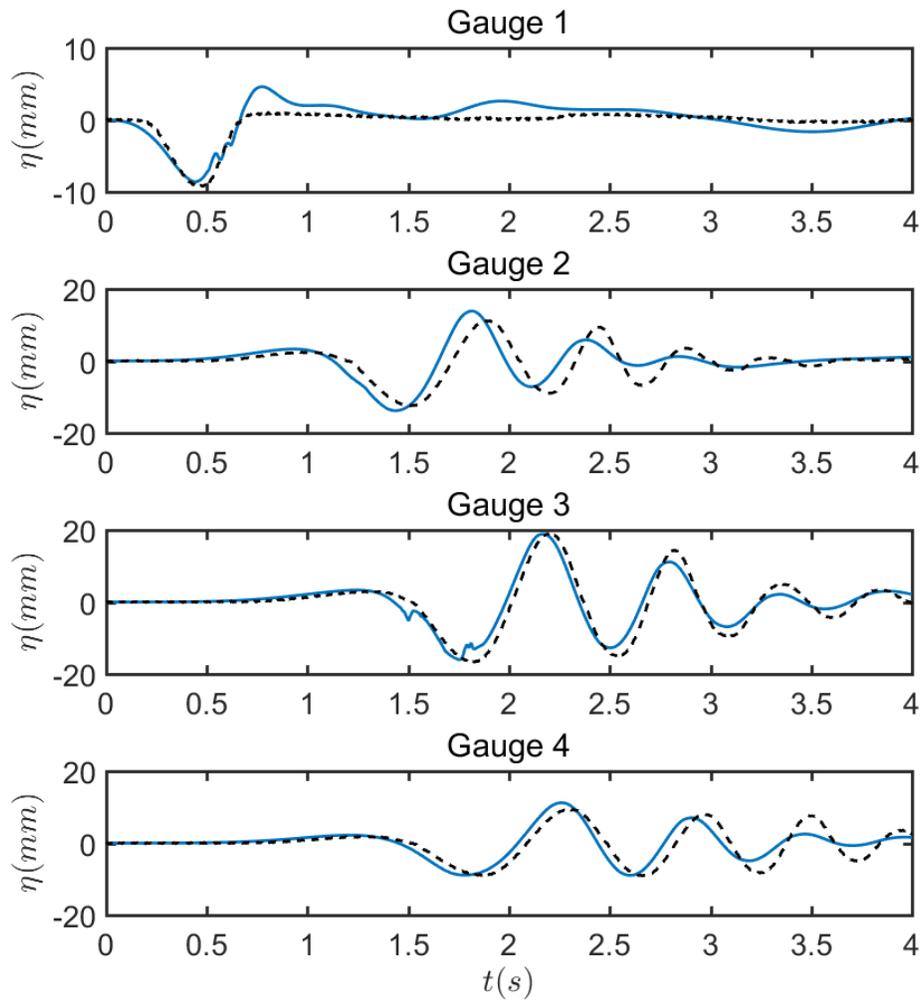
Figure 9: Benchmark 2: Comparison of surface elevation between numerical results of the case $d = 80$ mm from NHWAVE and experimental data at locations of (x,y)= $(0.617, 0)$, $(1.469, 350)$, $(1.929, 0)$, $(1.919, 500)$ in meters. Solid blue lines represent numerical results and dashed black lines represent experimental data.
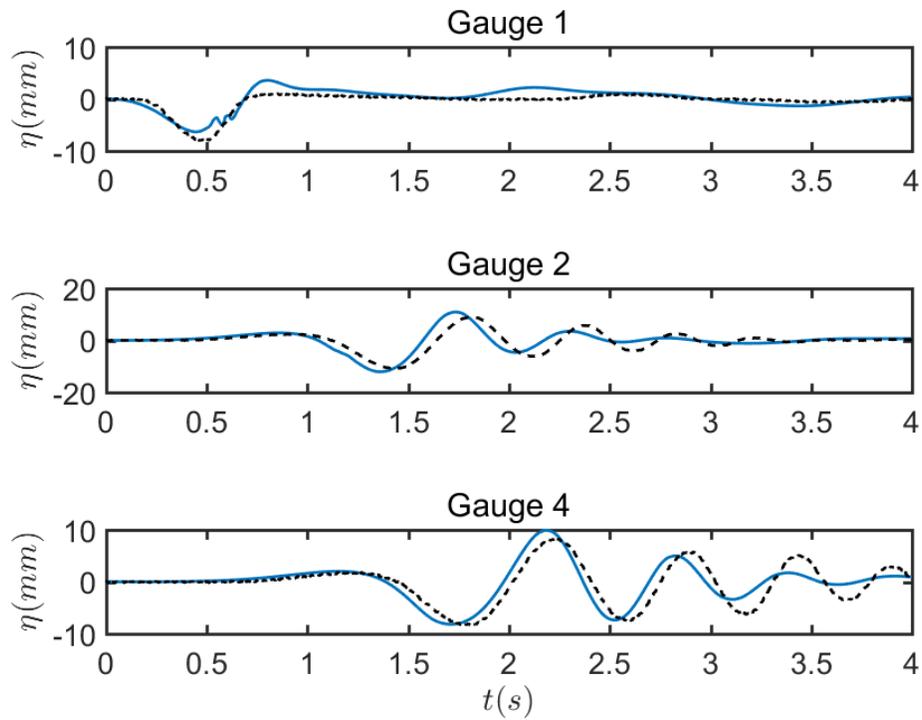
Figure 10: Benchmark 2: Comparison of surface elevation between numerical results of the case $d = 100$ mm from NHWAVE and experimental data at locations of (x,y)= $(0.696, 0)$, $(1.469, 350)$, $(1.919, 500)$ in meters. Solid blue lines represent numerical results and dashed black lines represent experimental data.
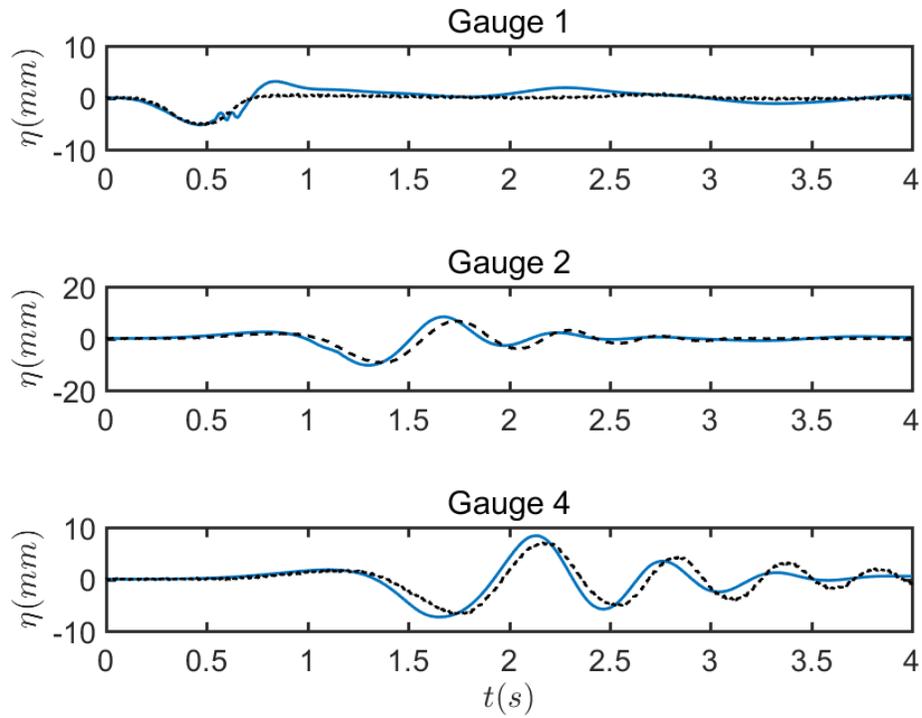
Figure 11: Benchmark 2: Comparison of surface elevation between numerical results of the case $d = 120$ mm from NHWAVE and experimental data at locations of (x,y)= $(0.763, 0)$, $(1.469, 350)$, $(1.919, 500)$ in meters. Solid blue lines represent numerical results and dashed black lines represent experimental data.
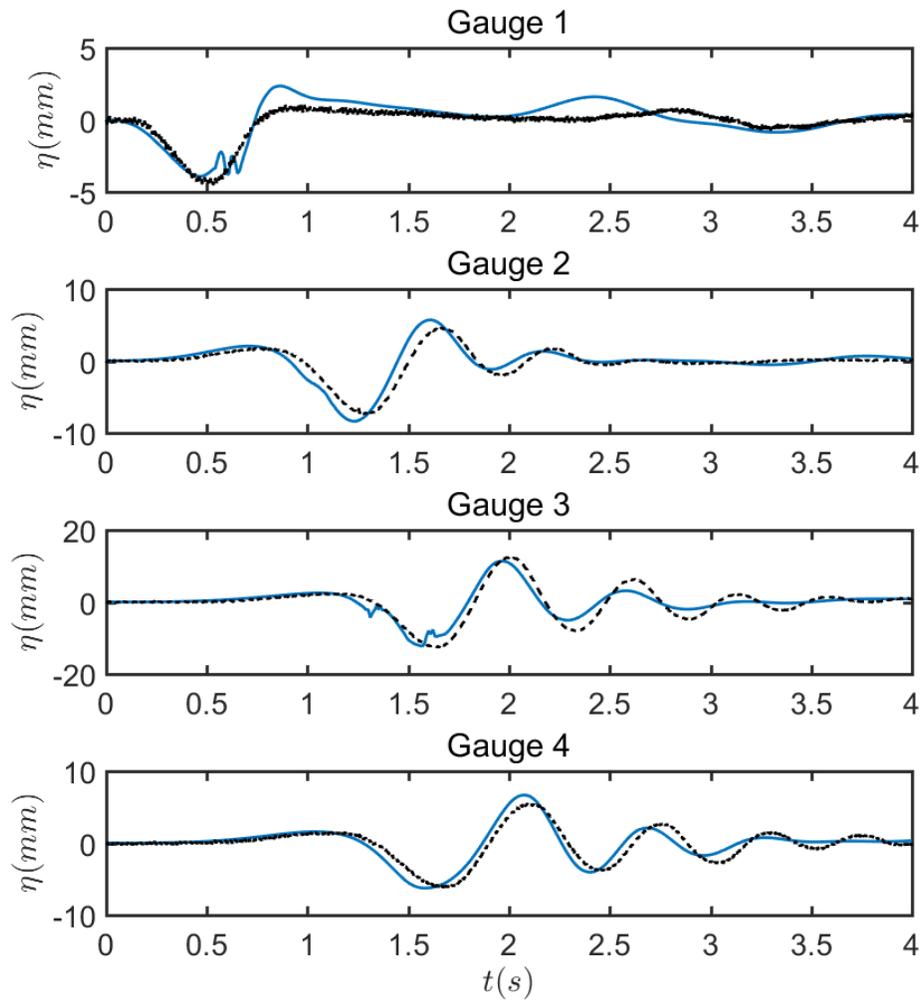
Figure 12: Benchmark 2: Comparison of surface elevation between numerical results of the case $d = 140$ mm from NHWAVE and experimental data at locations of (x,y)= $(0.846, 0)$, $(1.469, 350)$, $(1.929, 0)$, $(1.919, 500)$ in meters. Solid blue lines represent numerical results and dashed black lines represent experimental data.
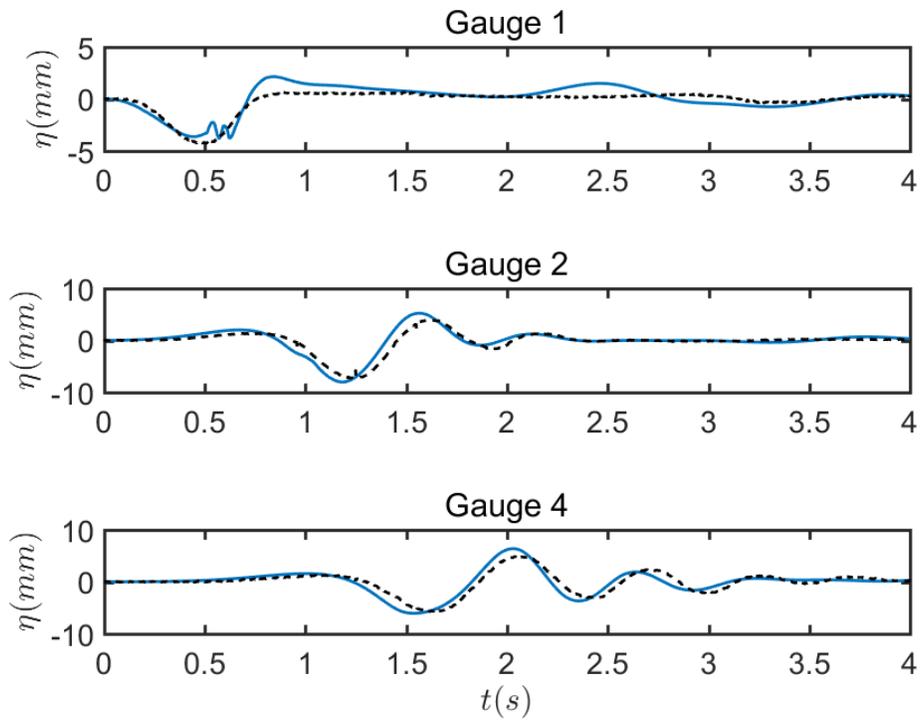
Figure 13: Benchmark 2: Comparison of surface elevation between numerical results of the case $d = 149$ mm from NHWAVE and experimental data at locations of (x,y)= $(0.877, 0)$, $(1.469, 350)$, $(1.919, 500)$ in meters. Solid blue lines represent numerical results and dashed black lines represent experimental data.
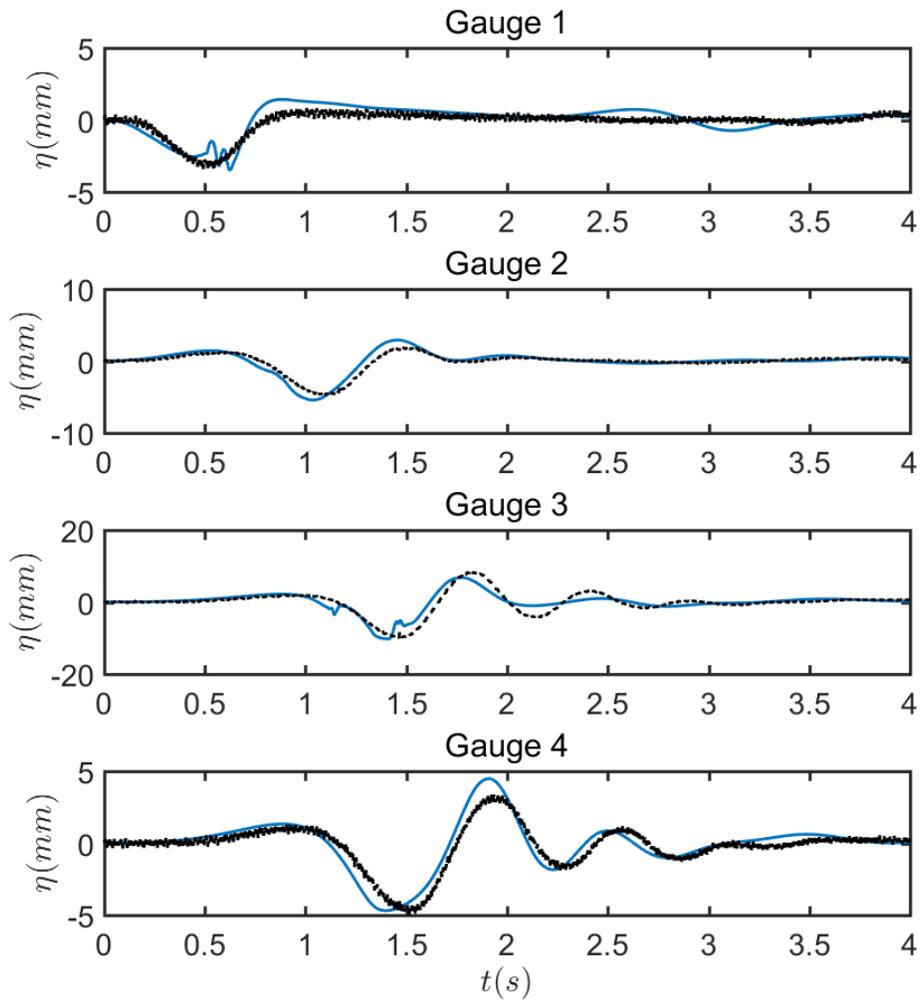
Figure 14: Benchmark 2: Comparison of surface elevation between numerical results of the case $d = 189$ mm from NHWAVE and experimental data at locations of (x,y)= $(1.017, 0)$, $(1.469, 350)$, $(1.929, 0)$, $(1.919, 500)$ in meters. Solid blue lines represent numerical results and dashed black lines represent experimental data.
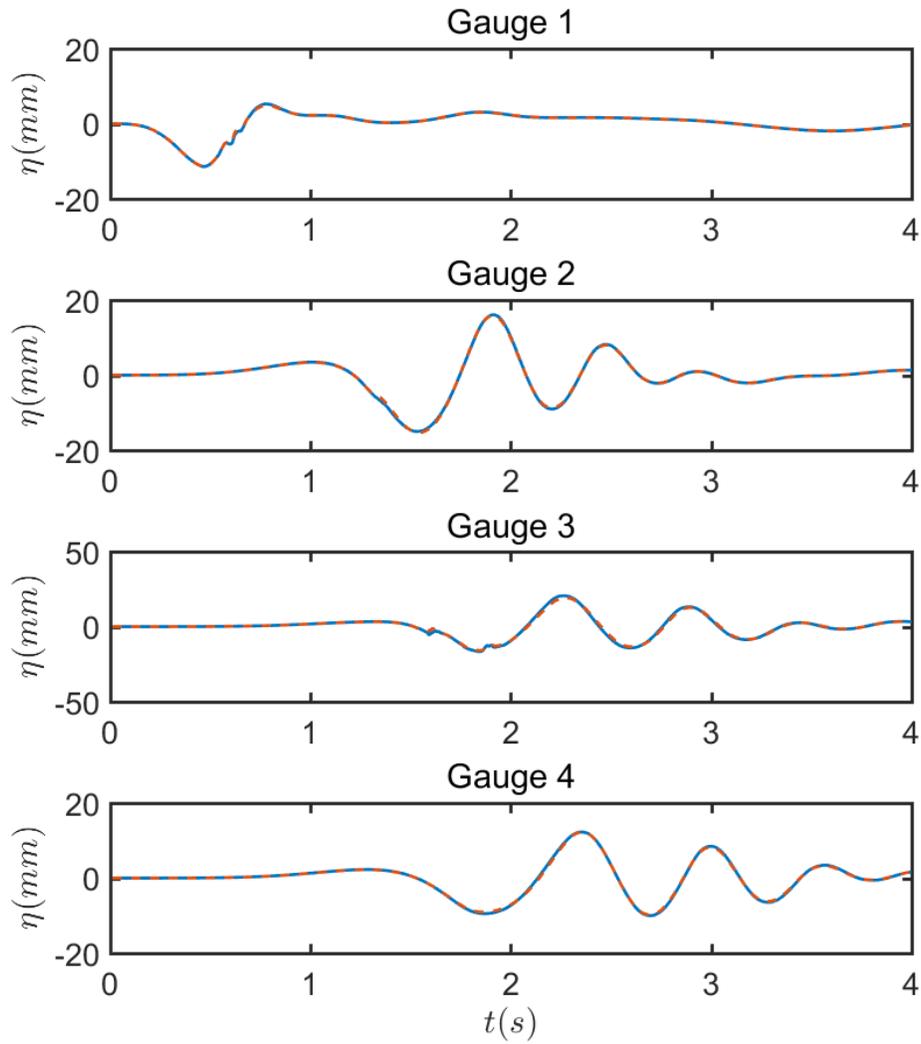
Figure 15: Comparison of results for case $d = 61$ mm between numerical solution and analytical solution for $\mathrm{d}h/\mathrm{d}t$ and $\mathrm{d}^2h/\mathrm{d}t^2$. Solid blue lines represent numerical solution and dashed red lines represent analytical solution.
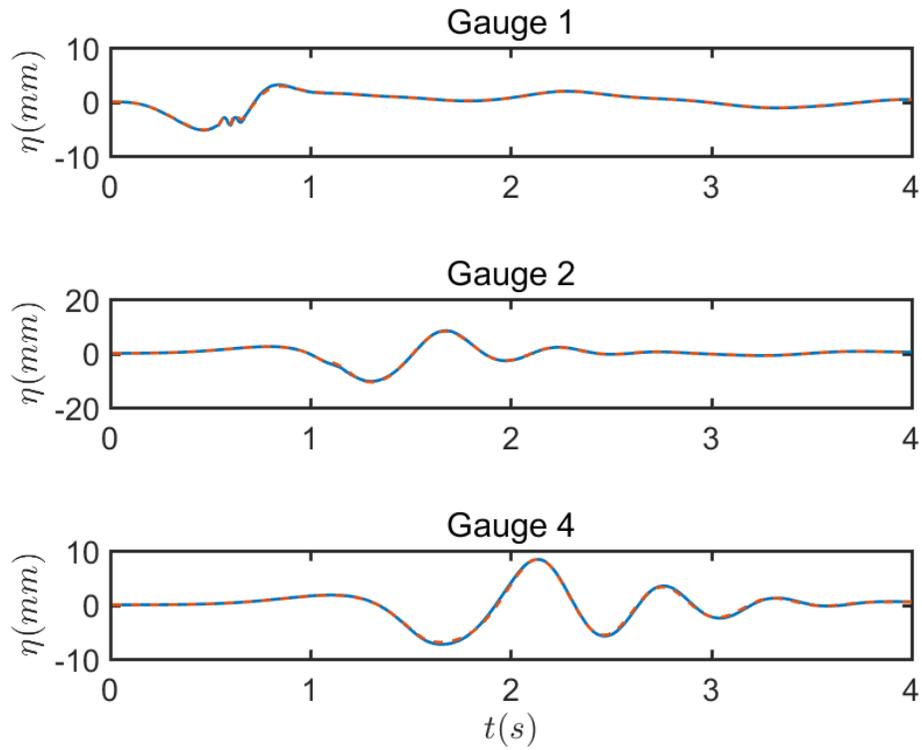
Figure 16: Comparison of results for case $d = 120$ mm between numerical solution and analytical solution for $\mathrm{d}h/\mathrm{d}t$ and $\mathrm{d}^2h/\mathrm{d}t^2$. Solid blue lines represent numerical solution and dashed red lines represent analytical solution.
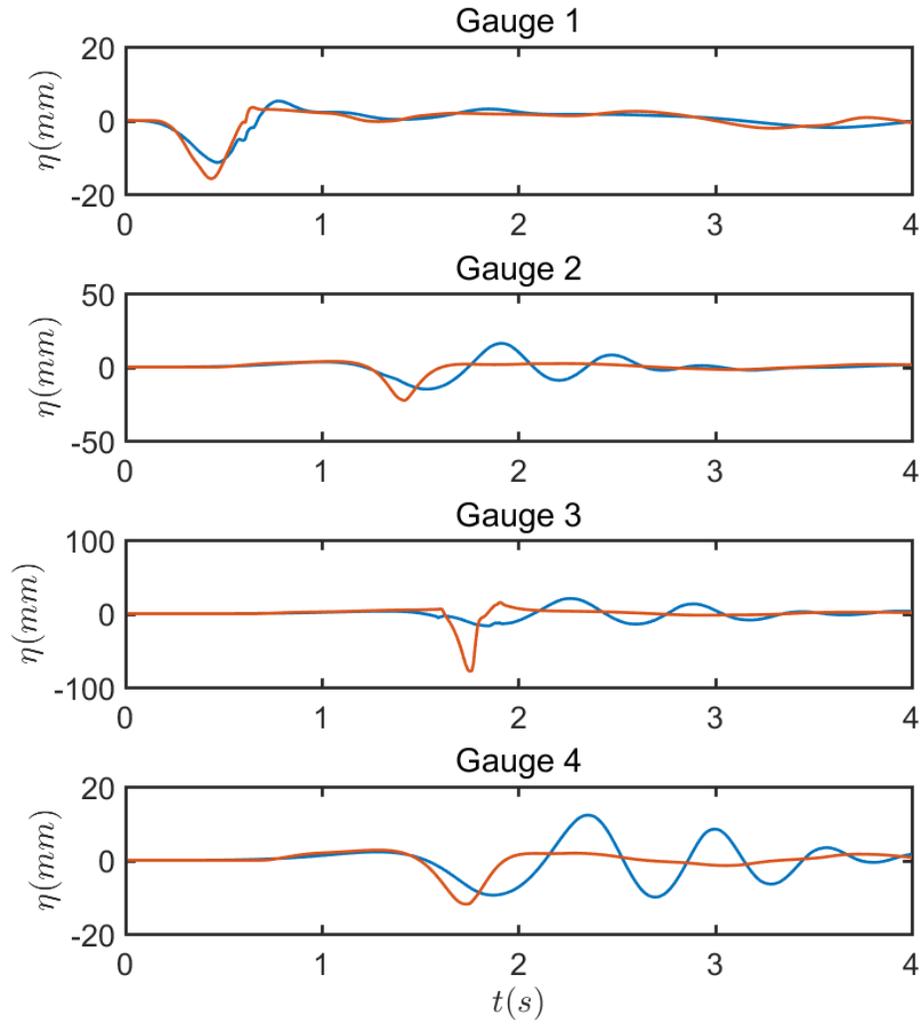
Figure 17: Comparison of results for case $d = 61$ mm between numerical solution with and without non-hydrostatic pressure. Blue lines represent numerical solution with non-hydrostatic pressure and red lines represent the solution without non-hydrostatic pressure.
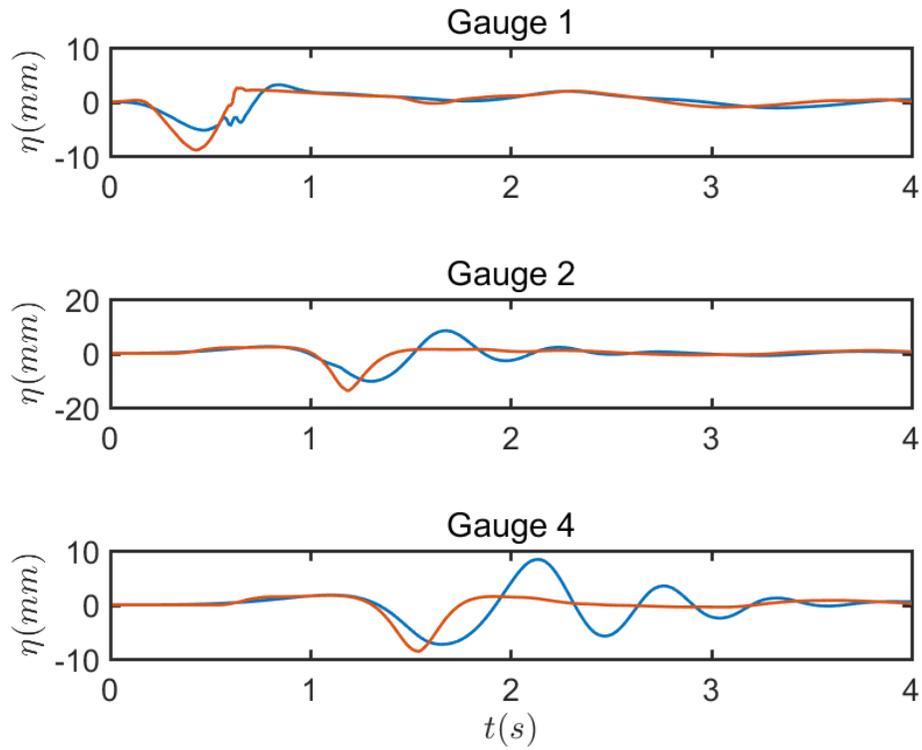
Figure 18: Comparison of results for case $d = 120$ mm between numerical solution with and without non-hydrostatic pressure. Blue lines represent numerical solution with non-hydrostatic pressure and red lines represent the solution without non-hydrostatic pressure.

3.3 Benchmark 3: Three-dimensional subaerial/submarine triangular solid block

Benchmark 3 is based on 3D laboratory experiments of Wu (2004) and Liu et al. (2005), of which a series of triangular blocks slide down a plane slope with an angle $\theta = 26.6°$ into water from a dry (subaerial) or wet (submarine) location. The depth of water is 2.44 m and the width of the wave tank is 3.7 m. The setup of the cases is shown in Figure 19. In this benchmark test, the triangle length $b = 0.91$ m, height $a = 0.455$ m and width $w = 0.61$ m, and two initial block locations $\Delta = 0.10$ m and -0.025 m are tested. The surface elevation recorded at two wave gauges located at $(x, y) = (1.83, 0)$ and $(1.2446, 0.635)$ m and runup measured at $y = 0.305$ m and 0.61 m, where x is the distance to the initial shoreline and y is the distance to the central cross-section. Data for the comparison was obtained from http://www1.udel.edu/kirby/landslide/problems/benchmark_3.html. The model configuration was NHWAVE with imposed solid bottom motion.
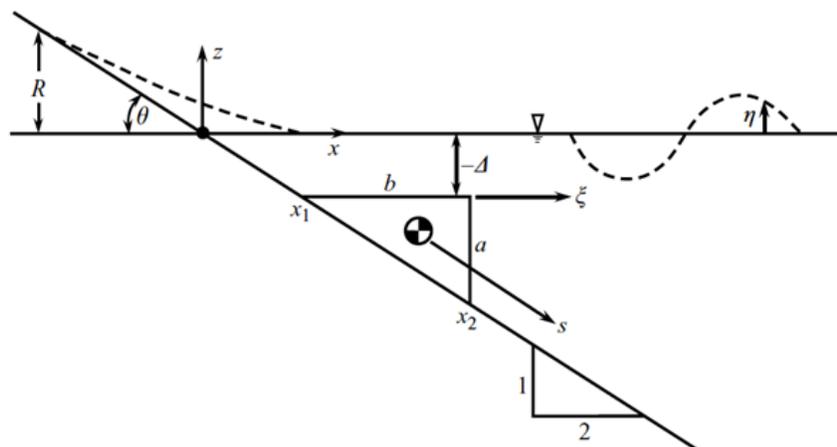
Figure 19: Sketch of main parameters for 3D subaerial/submarine triangular landslide benchmark.(From Liu et al., 2005)

In the simulation, a uniform grid size of 0.02 m is used to discretize half the mirror-symmetric computational domain of 10×3.6 m and the water depth is divided into 3 layers. Here, since the initial shape of the wedge has vertical faces which may hard to be captured by the current model, we use a smoothed shape to represent the slide, as shown in Figure 20. The vertical faces of the wedge are tilted a little and then smoothed with a cosine shape by multiplying $0.5\,(1 + \cos(\pi x/2e))$ or $0.5\,(1 + \cos(\pi y/2f))$ in $x - z$ plane and $y - z$ plane, respectively, where $e = 0.2$ m and $f = 0.1$ m in this case.

The motions of the block for both subaerial and submarine cases are given by a function of time, i.e., $s = at^3 + bt^2 + c$, where the coefficients of the polynomial list in Table 2.

Figure 21 and 22 show the comparison of surface elevation and runup at 4 gauges for case $\Delta = 0.10$ m and case $\Delta = -0.025$ m between numerical results and experimental data.
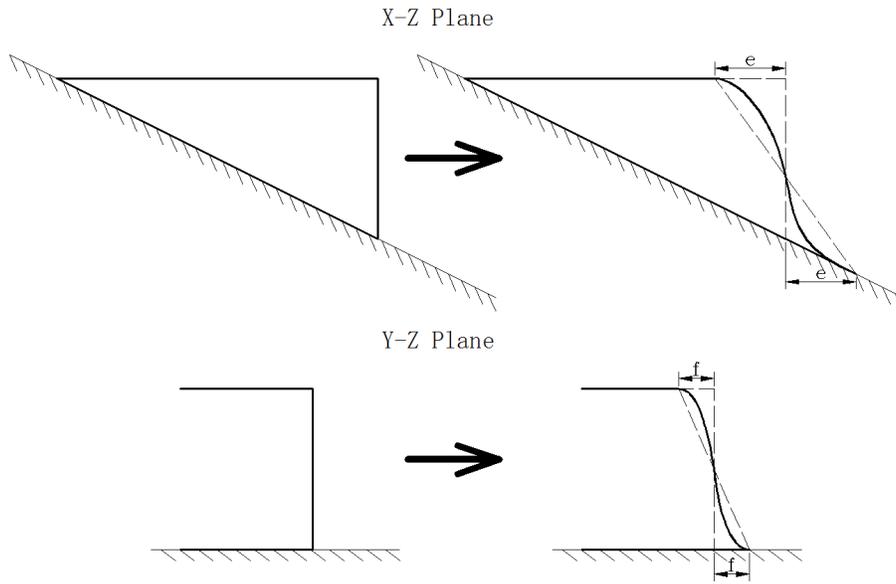
Figure 20: Smoothness of triangular block

Δ	a	b	c
0.10 m	-0.097588	0.759361	0.078766
-0.025 m	-0.085808	0.734798	-0.034346

Table 2: Coefficients of polynomial $s = at^3 + bt^2 + c$.
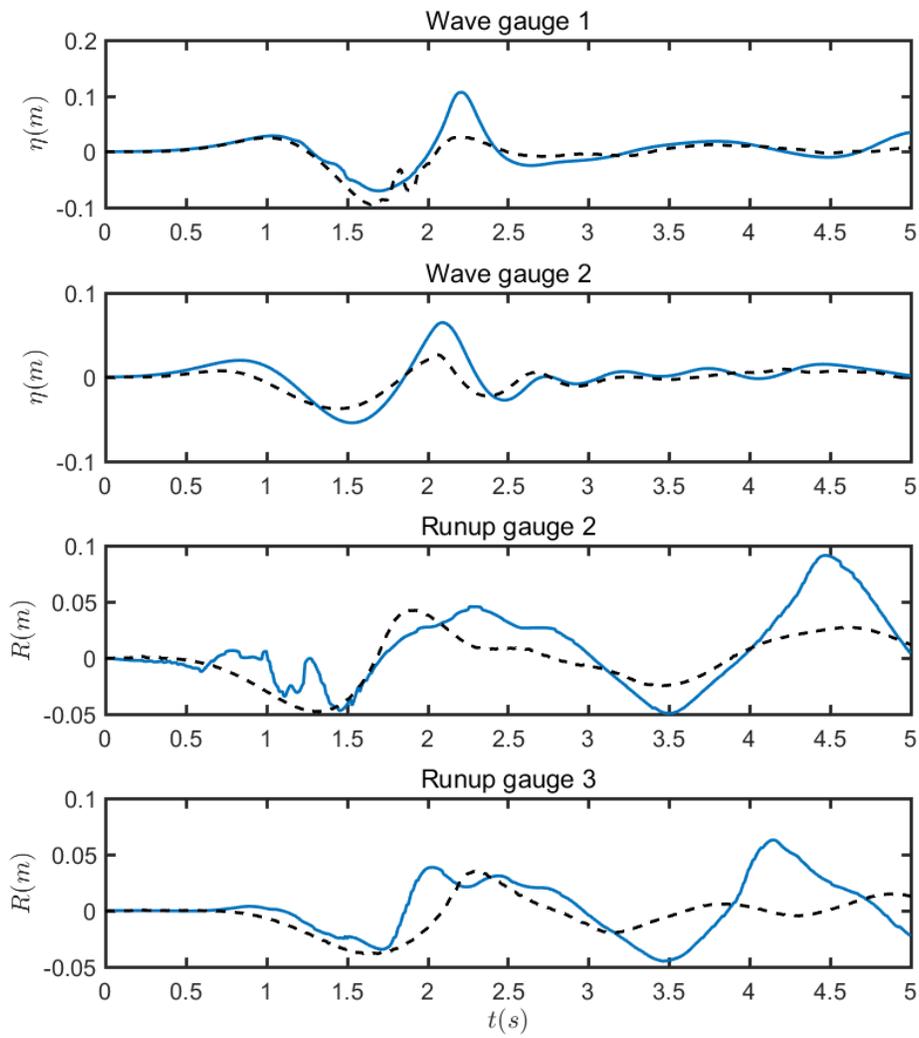
Figure 21: Benchmark 3: Comparison of surface elevation and runup at 4 gauges for case $\Delta = 0.10$ m between numerical results and experimental data. Solid blue lines represent numerical results and dashed black lines represent experimental data.
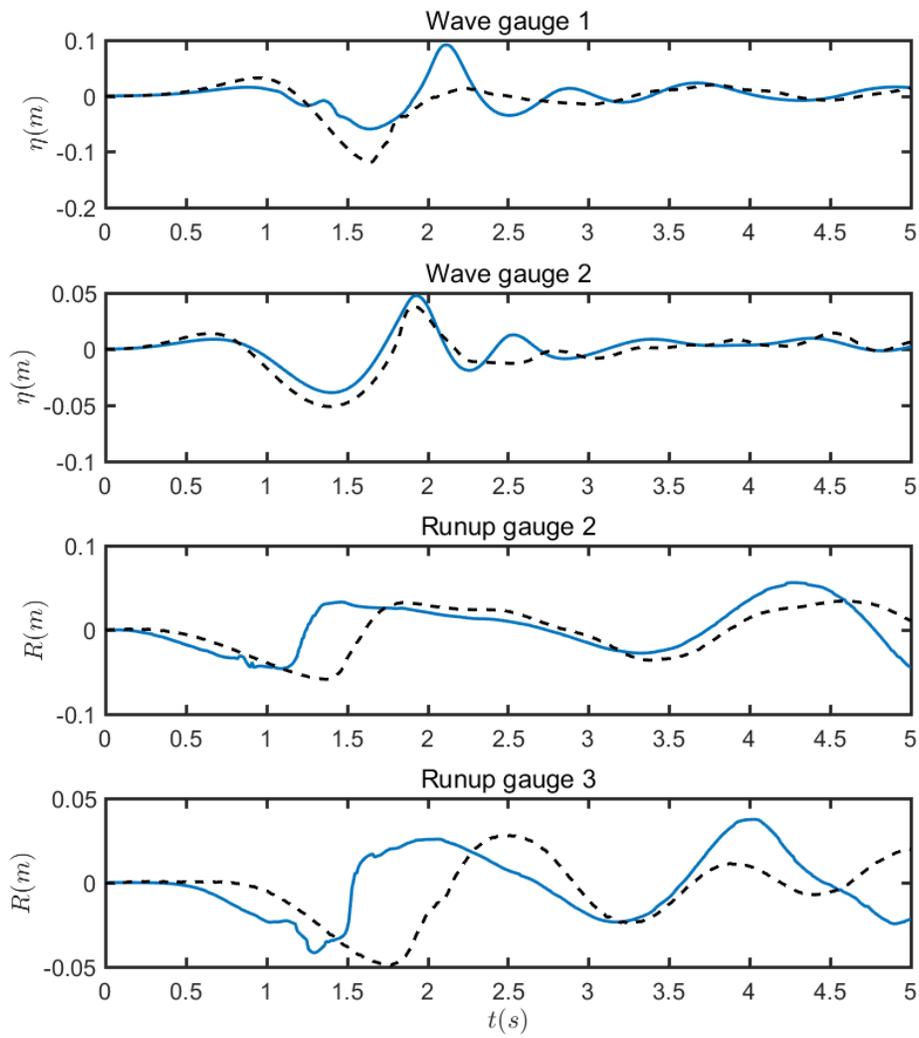
Figure 22: Benchmark 3: Comparison of surface elevation and runup at 4 gauges for case $\Delta = -0.025$ m between numerical results and experimental data. Solid blue lines represent numerical results and dashed black lines represent experimental data.

3.4 Benchmark 4: Two-dimensional submarine granular landslide

Benchmark 4 is based on 2D laboratory experiments carried out by Kimmoun and Dupont and described in Grilli et al. (2016). The experiments were performed in the Ecole Centrale de Marseille's (IRPHE) precision tank, for a series of triangular submarine cavities filled with glass beads, released by lifting a sluice gate and moving down a plane slope into water. Figures 23 and 24 show pictures and sketches of the experimental set-up.

We simulated experiment for test 17 using both the heavy Newtonian fluid landslide model of Kirby et al. (2016), the granular landslide model of Ma et al. (2015) and the water-sediment mixture landslide model in NHWAVE. Fig. 25 shows the comparison of simulated and measured free surface elevations at four wave gauges using the granular landslide model. In this simulation, the computational domain is discretized by 250 grid cells in along-flume direction with grid size of 2.5 cm. Based on laboratory measurements, the internal friction angle ϕ_{int} is 41° and ϕ_{bed} is 23.3^o. The λ parameter introduced in the granular flow equations is taken as 0.6. It is clearly observed that the simulations agree fairly well with the measurements, indicating that the model can reasonably capture the granular slide motion and the generation of impulsive waves. Fig. 26 shows numerical results with and without non-hydrostatic pressure, and apparently the model without non-hydrostatic pressure performs badly for this case. The numerical results using the viscous landslide model shown in Fig. 27 agree well with the measured data.

Fig. 28 shows the comparison of simulated and measured free surface elevations at four wave gauges using the water-sediment mixture landslide model. In this simulation, the computational domain is discretized by 250 grid cells in along-flume direction with grid size of 2.5 cm. 20 vertical sigma levels are used to capture the landslide motion. Generally, the wave heights are overestimated. The results get better in the far field wave gauges. Fig. 29 plots the geometry of the landslides at $t = 0.02, 0.17, 0.32, 0.47 s$, which is represented by the contour lines with volumetric sediment concentration of 0.001. It is found that the model is capable of capturing the bulge of the slide front and reasonably predicting the locations of the slide front. The flow fields show that a large-scale vorticity is generated at the slide front as the landslide moves downward along the slope.

Figure 23: Set-up for laboratory experiments of tsunami generation by underwater slides made of glass beads performed in IRPHE's precision tank with useful length l = 6.27 m, width w = 0.25 m, and water depth h = 0.330 m. Upon release, beads are moving down a $\theta = 35°$ slope. (a) Longitudinal cross section with marked location of sluice gate and 4 wave gages (WG1, WG2, WG3, WG4). (b,c) Zoom-in on side- and cross-section views of slope and sluice gate (dimensions marked in mm). (d) Picture of experimental set-up around slope and sluice gate.
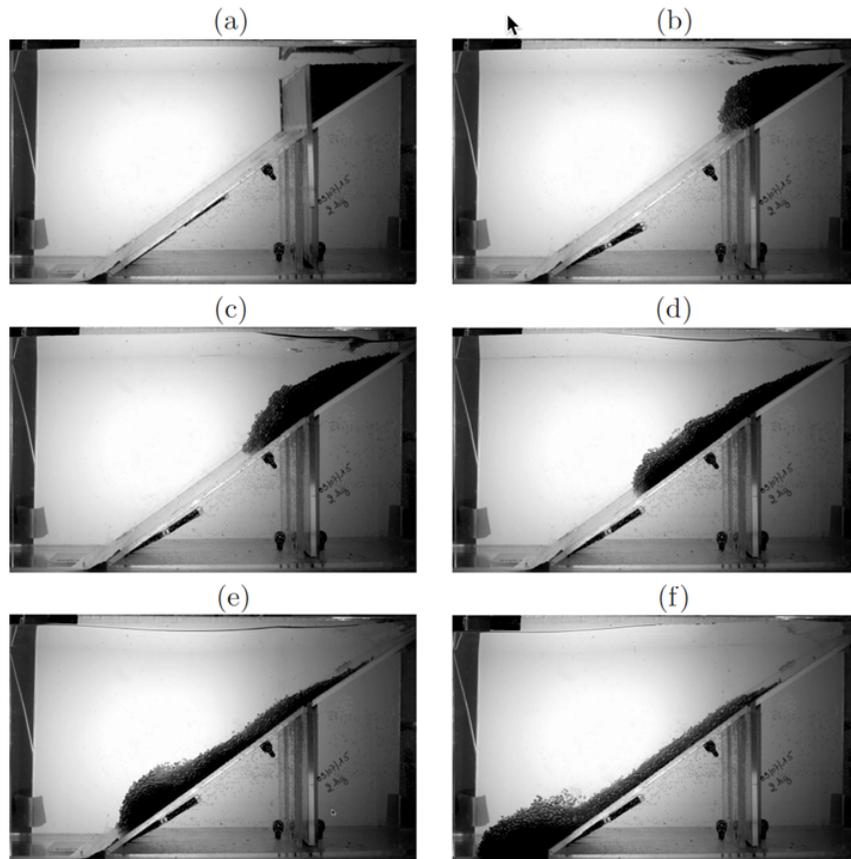
Figure 24: Snapshots of laboratory experiments of tsunami generation by underwater slide made of glass beads, for $h = 0.330$ m; $d_b = 4$ mm, $W_b = 2$ kg, at times $t =$ (a) -0.105; (b) 0.02; (c) 0.17; (d) 0.32; (e) 0.47; and (f) 0.62 s. Note, glass beads are initially stored within the glass bead reservoir with the sluice gate up; at later times, after the gate is withdrawn, the deforming slide moves down the $35°$ slope while the free surface is deformed. The slope is smooth, with no glued beads. The starting time of experiments $t = 0$ is defined when the gate has just withdrawn into its cavity.
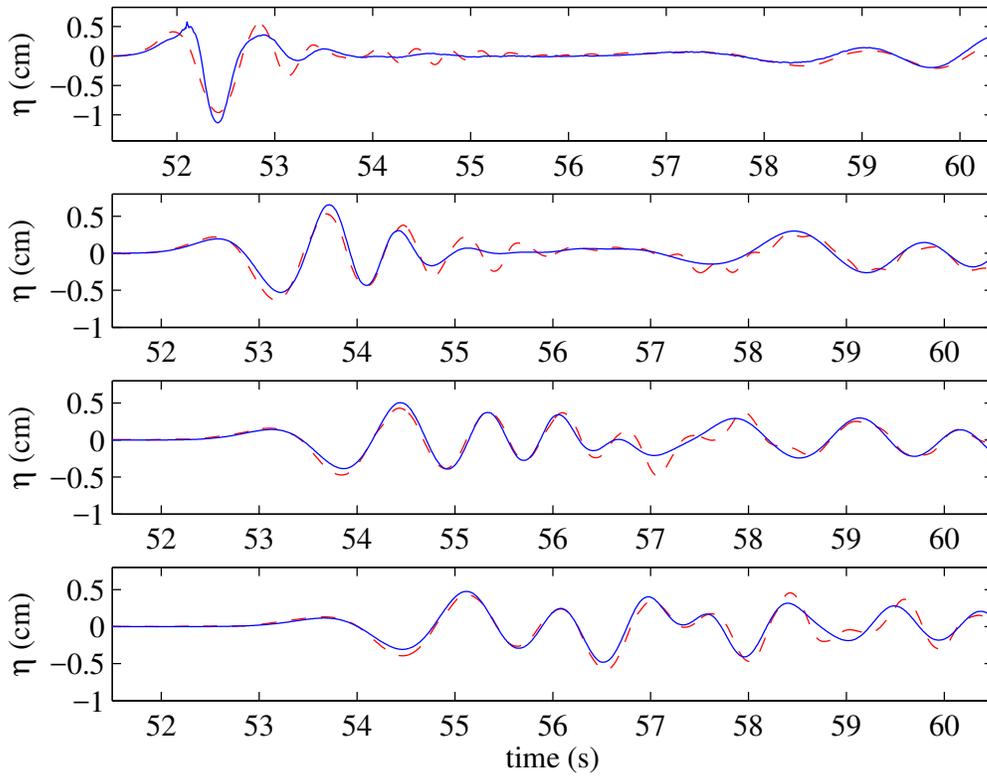
Figure 25: Benchmark 4: Model-data comparisons of free surface elevations at four wave gauges for test 17 using the granular landslide model.
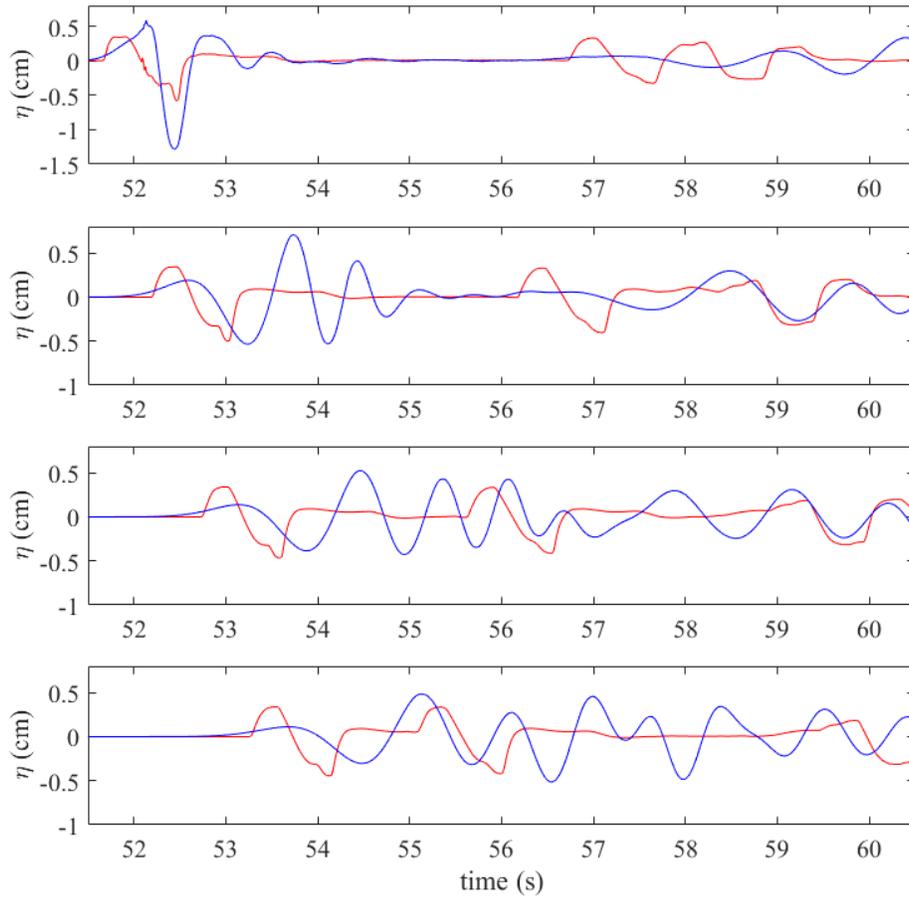
Figure 26: Benchmark 4: Model-data comparisons of free surface elevations at four gauges with and without non-hydrostatic pressure. Blue lines represent numerical solution with non-hydrostatic pressure and red lines represent the solution without non-hydrostatic pressure.
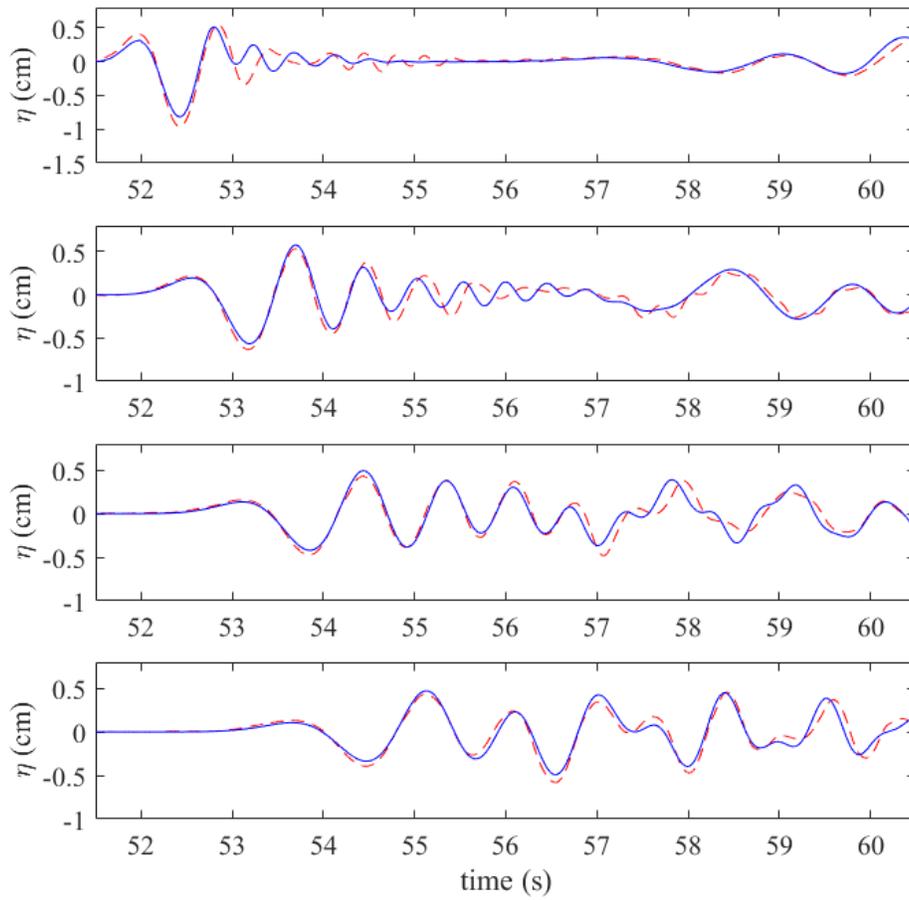
Figure 27: Benchmark 4: Model-data comparisons of free surface elevations at four wave gauges for test 17 using the viscous landslide model.
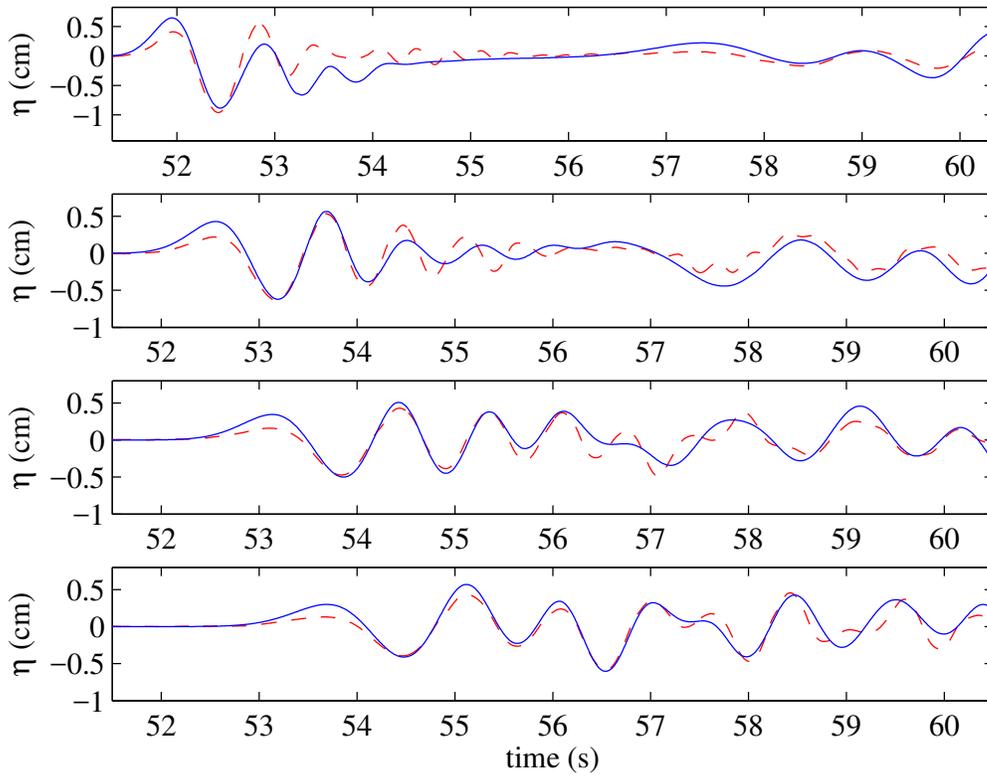
Figure 28: Benchmark 4: Model-data comparisons of free surface elevations at four wave gauges for test 17 using the water-sediment mixture landslide model.
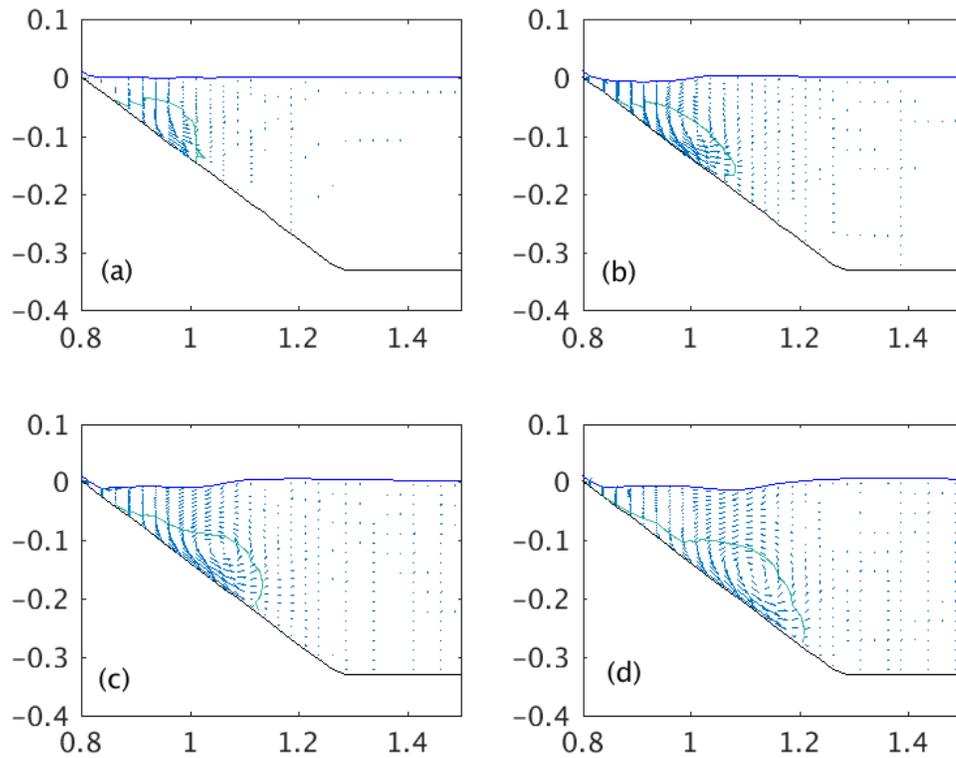
Figure 29: Benchmark 4: Slide motions and flow fields using the water-sediment mixture landslide model at (a) t = 0.02 s; (b) t = 0.17 s; (c) t = 0.32 s; and (d) t = 0.47 s.
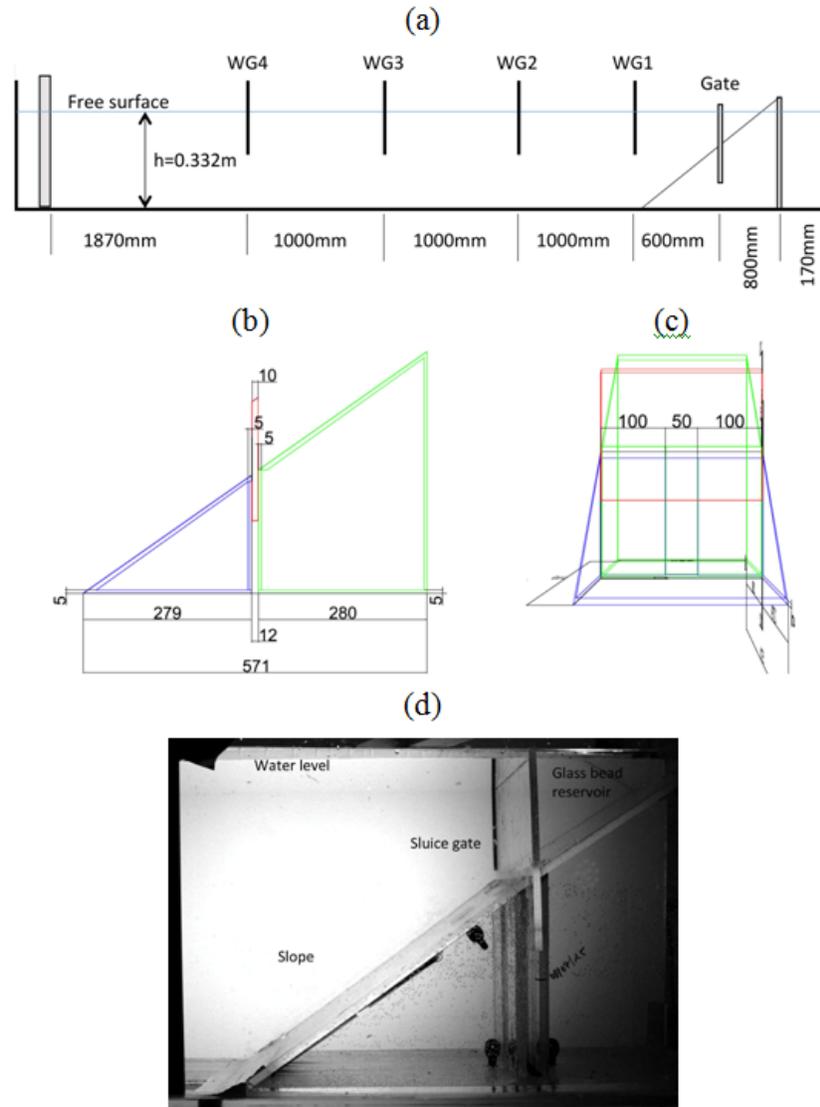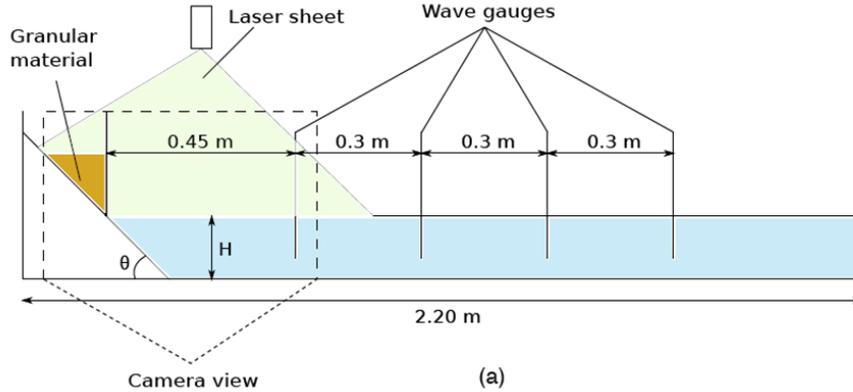
Figure 30: Set-up for laboratory experiments of tsunami generation by subaerial slides made of glass beads performed in IRPHE's precision tank of (useful) length $l = 2.20$ m, width $w = 0.2$ m, and water depth $H = 0.150$ m. Upon release, beads are moving down a slope of $\theta = 45°$. The slide shape and water motion are recorded with high speed video camera and laser PIV, respectively. Surface elevations are recorded at 4 wave gages (WG1, WG2, WG3, WG4) marked on the figure.

3.5 Benchmark 5: Two-dimensional subaerial granular landslide

This benchmark problem is based on the 2D laboratory experiments of Viroulet et al. (2014) in a small tank at Ecole Centrale de Marseille's (IRPHE; Marseille, France), for a series of triangular subaerial cavities filled with dry glass beads of diameter D and density $\rho_s = 2,500$ kg/m^3, released by lifting a sluice gate and moving down a plane $45°$ slope into water. Figures 30 - 31 show pictures and sketches of the experimental set-up.

The experimental set-up used by Viroulet et al. (2014) is shown in Figure 30. It consists of a wave tank, 2.2 m long, 0.4 m high, and 0.2 m wide. A granular slide is initially retained by a vertical gate on the dry slope. At the beginning of the experiment, the gate is suddenly lowered. In the numerical model, it should be assumed that the gate release velocity is large enough to neglect the time it takes the gate to withdraw. The initial slide shape will be assumed to have a triangular cross-section over the width of the tank, with down-tank length L, and front face height $B = L$ as the slope angle is $45°$. In all cases, the front face of the granular slide touches the free surface at $t = 0$.

Two test cases are considered in this benchmark, which are referred to as Case 1 and Case 2 in the result files names. The initial conditions for each case are, respectively: Case 1 : D = 1.5 mm, H = 14.8 cm, L = 11cm; Case 2 : D = 10 mm, H = 15 cm, L = 13.5 cm.

In the simulations, the computational domain is discretized by 220 grid cells with grid size of 1.0 cm. The granular landslide model is employed to simulate the slide motion. The parameters

36
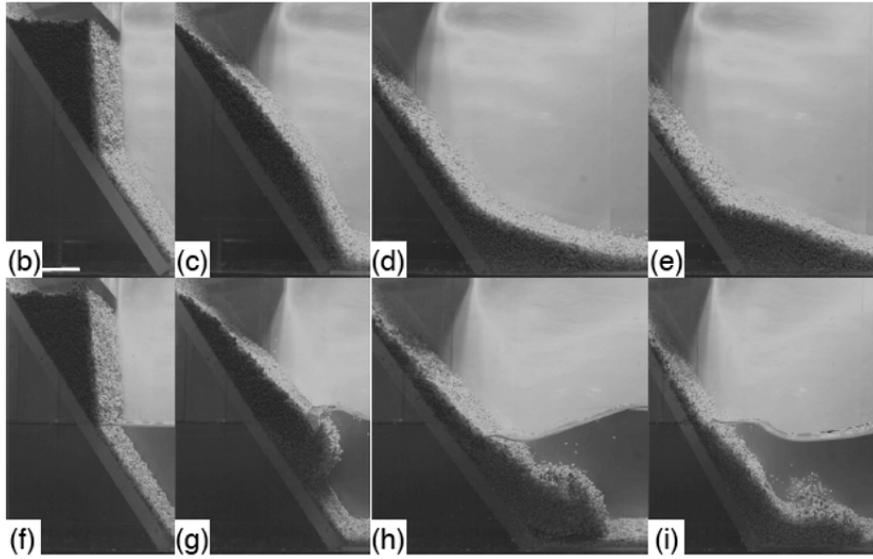
Figure 31: Shape of glass bead slide recorded with a video camera every 0.2 s (white bar in (b) is 5 cm long).

used in the simulations are: $\phi_{bed} = 25.7°$, $\lambda = 0.45$ for case 1 and $\phi_{bed} = 21.3°$, $\lambda = 0.40$ for case 2, respectively. Figs. 32 and 33 show the comparisons of free surface elevations at four wave gauges for case 1 and 2, respectively. The agreements between simulations and measurements are quite good.
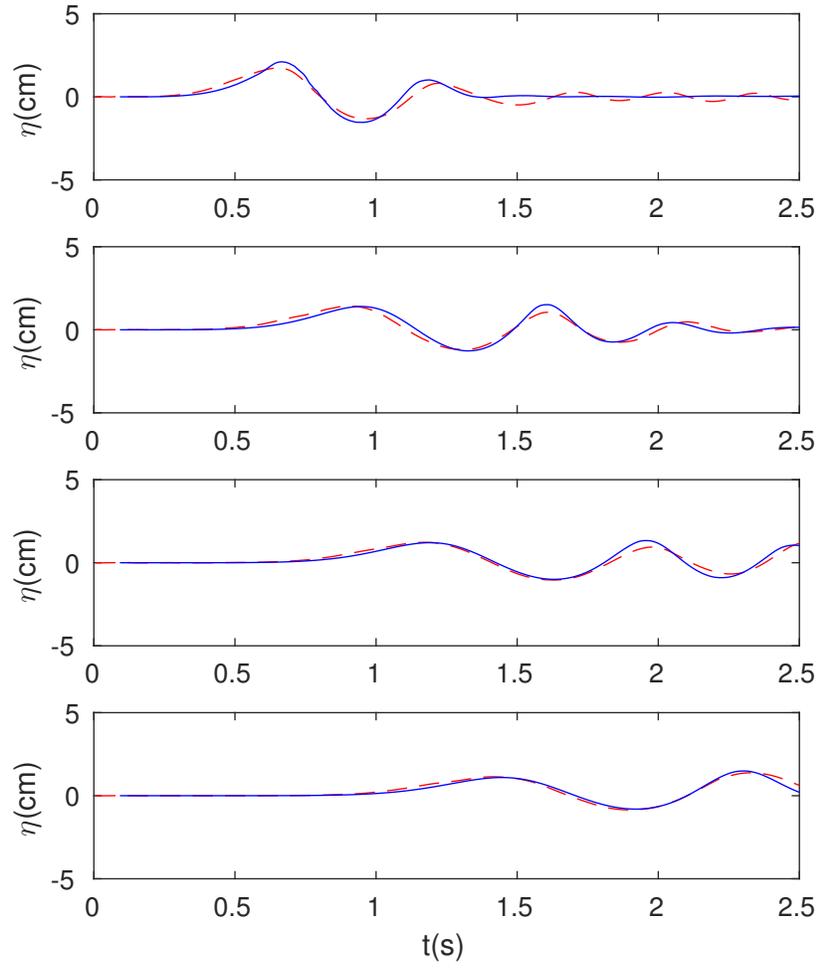
Figure 32: Benchmark 5: Model-data comparisons of free surface elevations at four wave gauges for case 1.
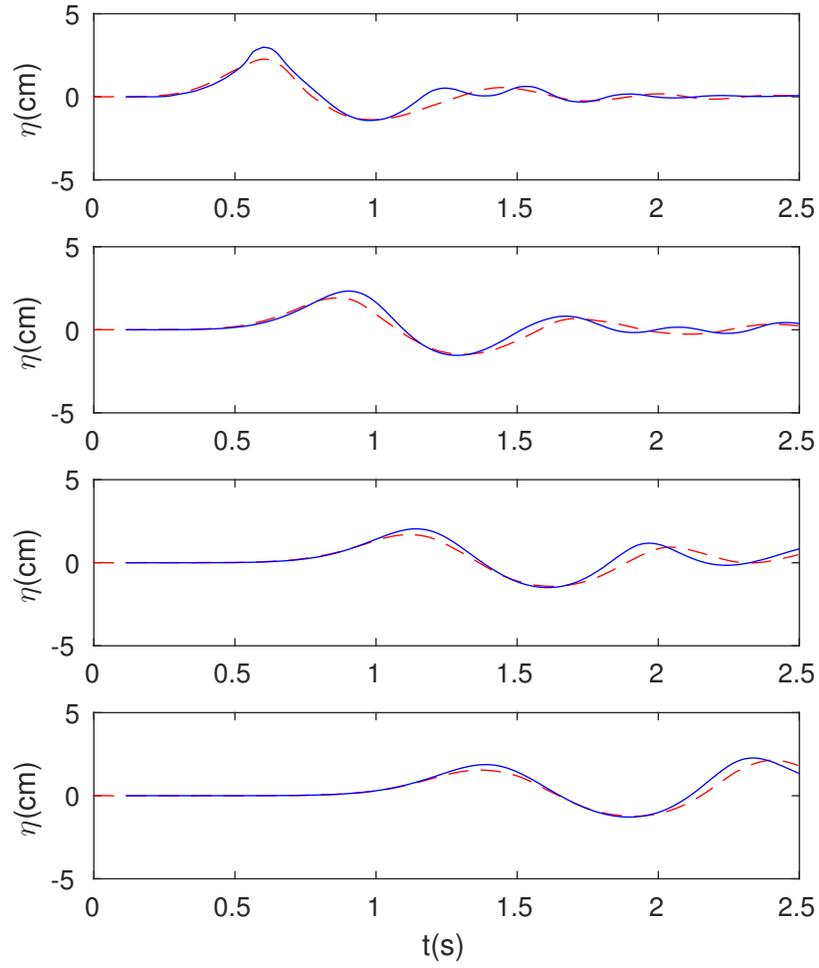
Figure 33: Benchmark 5: Model-data comparisons of free surface elevations at four wave gauges for case 2.
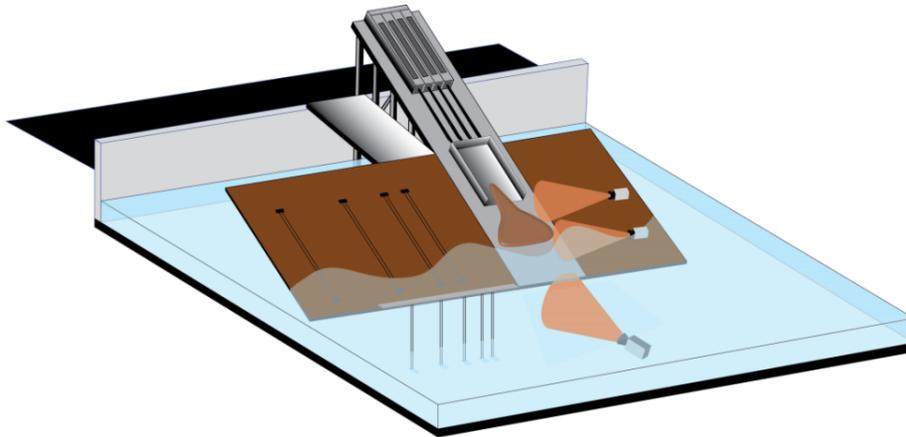
Figure 34: Landslide tsunami generator setup

3.6 Benchmark 6: Three-dimensional subaerial granular landslide

Benchmark 6 simulates rapid entry of a narrow slide into an unconstrained, 3D water body, reported by Mohammed and Fritz (2012). The landslide tsunami experiments were conducted in the tsunami wave basin at Oregon State University in Corvallis. The landslides are deployed off a plane slope built on one end of the wave basin as shown in Figure 34. Data for this comparison was obtained from http://www1.udel.edu/kirby/landslide/problems/benchmark_6.html. The NHWAVE+granular slide model was used to carry out the simulation.

The landslide material is deployed in a box measuring 2.1m × 1.2m × 0.3m, with a volume of 0.756 m^3 and weight of approximately 1360 kg.

The plane slope has a slope angle of 27.1° corresponding to a slope of 1 vertical to 2 horizontal. Two coordinate systems are defined to characterize the slide motion and wave propagation independently. Both the coordinate systems can be unified through the location of the shoreline, which is dependent on the water depth. The wave gauge locations in the basin with reference to the toe of the slope is shown in Figure 35. The slope coordinate system x_s and the wave gauge coordinate system x is shown in Figure 36 for a reference water depth of $h = 0.6$ m. The locations of the wave gauges are with reference to the toe of the slope shown in Figure 35. The toe and the shoreline can be related to each other knowing the slope angle of the hill slope as shown in Figure 36. Similarly, the shoreline location with reference to the slope coordinate system can be related to the water depth as shown in Figure 36.

The wave gauges numbered by indices 1-25 in the wave basin are located at (x, y) locations in the tsunami wave basin with reference to the hill slope toe and the wave basin coordinate system as shown in Table 3.

Figure 35: Wave gauge locations in the wave basin.

Figure 36: Two coordinate systems x_s and x shown for the slide and wave measurements. The y-direction is considered to be perpendicular outside the image.

41

Table 3: Wave gauge location with reference to the toe.

$WG\#$	x (m)	y (m)
1	24.1	0
2	24.1	2.108
3	14.0	0.0
4	14.0	1.225
5	14.0	3.232
6	14.0	5.374
7	8.5	0.0
8	8.5	0.744
9	8.5	1.962
10	8.5	3.236
11	8.5	4.907
12	5.12	0.0
13	5.12	0.448
14	5.12	1.182
15	5.12	1.965
16	5.12	2.956
17	5.12	5.12
18	5.12	8.868
19	3.9	2.252
20	3.9	3.9
21	3.9	6.755
	Runup Wave Gauges	
22	0	2.0
23	0	2.6
24	0	3.8
25	0	5.6

In the simulation, the computational domain size is 48 m in length and 28 m in width, discretized by 960 × 560 grid cells. Three vertical levels are employed to simulate the upper-layer water motion. Slightly different from the laboratory setup, the hillslope covers the whole width of the computational domain with x ¡ 8.13 m. The landslide is released in the middle of the hillslope at y = 14.0 m. The granular parameters are chosen to be the same as those in the experiment with $\phi_{int} = 41°$ and $\phi_{bed} = 23°$. The parameter λ is taken to be 0.0 above the water and 0.35 after the landslide enters the water column. We validate the model by comparing the tsunami waves at 20 wave gauges displayed in Fig. 35. Figs. 37 - 41 show the comparisons of free surface elevations at 20 wave gauges. Generally, the model simulates the tsunami waves well, although the wave heights are overestimated in the generating area close to the shoreline. Three reasons may be used to explain this over- prediction: (1) In the current model, the lower-layer landslide and upper-layer water remain in contact, thus the formation of air cavity during landslide impact is not captured; (2) the current model does not account for the increase of Coulomb friction due to the change of curvature at the transition of the slope; (3) the model slightly overpredicts the landslide height at the impact. In the far field, the overestimation of wave height decreases and the simulated tsunami waves match well with the measurements.

Figure 37: Benchmark 6: Model-data comparisons of tsunami waves for stations 1 to 4.

Figure 38: Benchmark 6: Model-data comparisons of tsunami waves for stations 5 to 8.

Figure 39: Benchmark 6: Model-data comparisons of tsunami waves for stations 9 to 12.
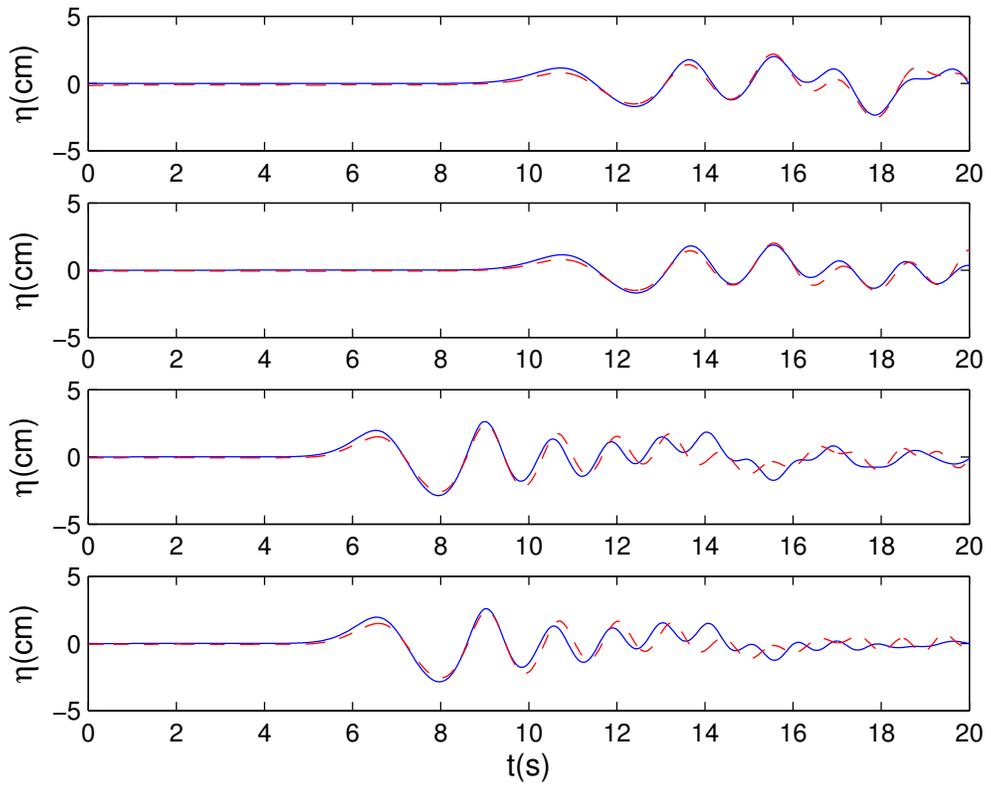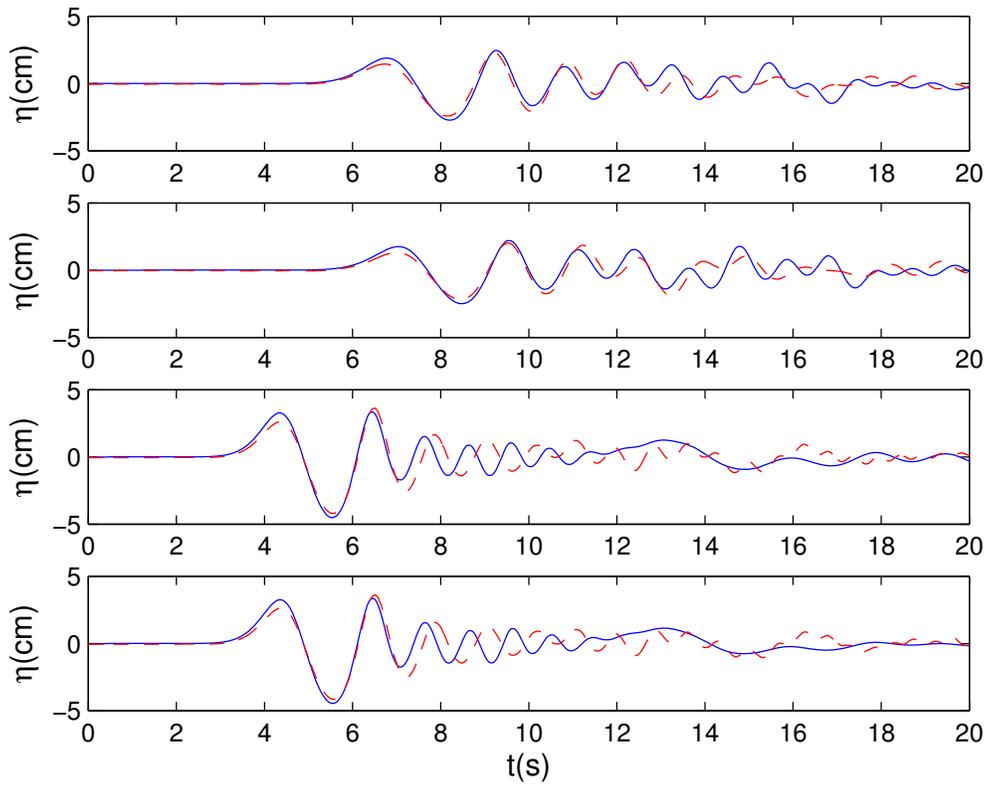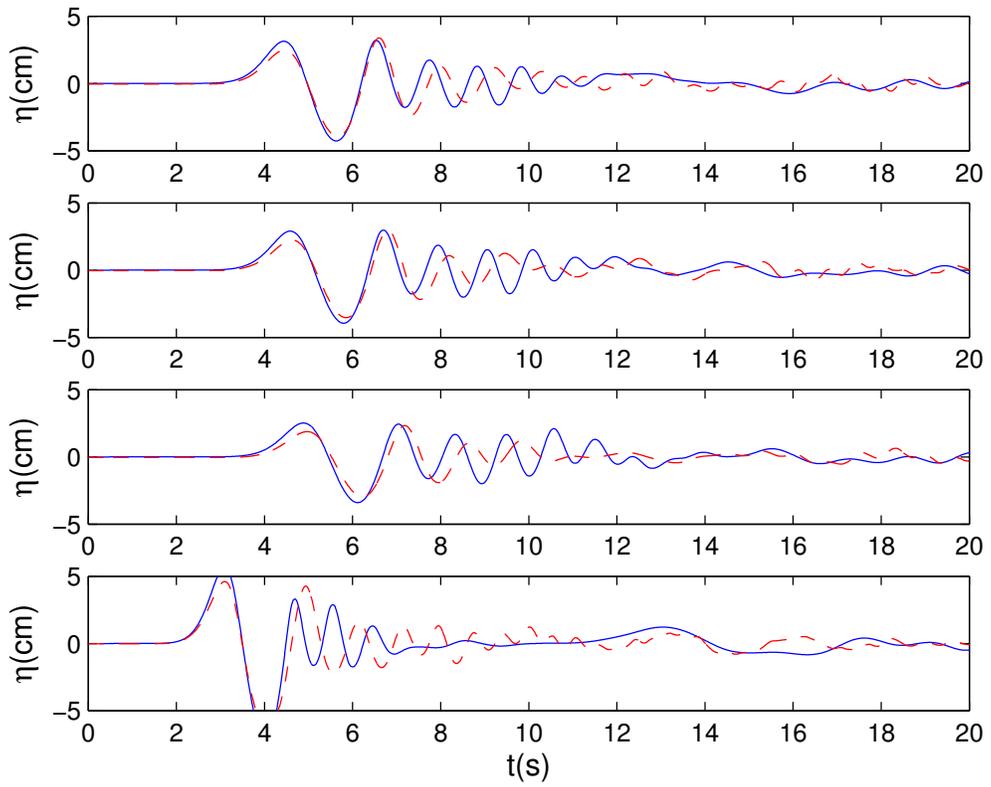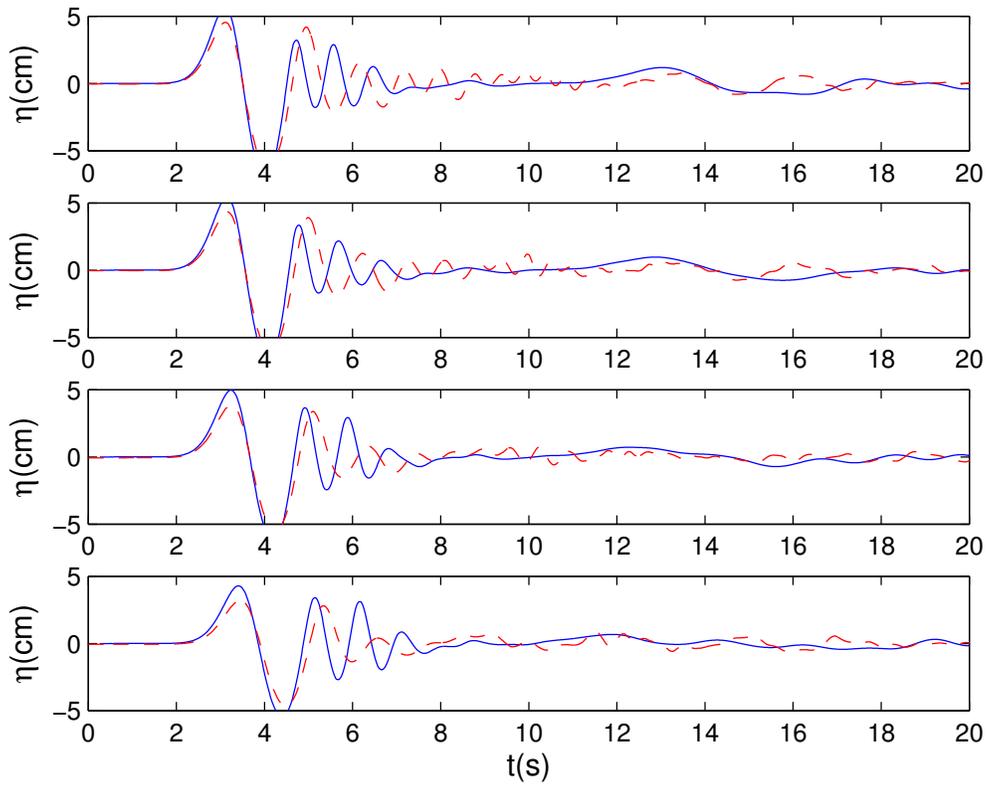
Figure 40: Benchmark 6: Model-data comparisons of tsunami waves for stations 13 to 16.
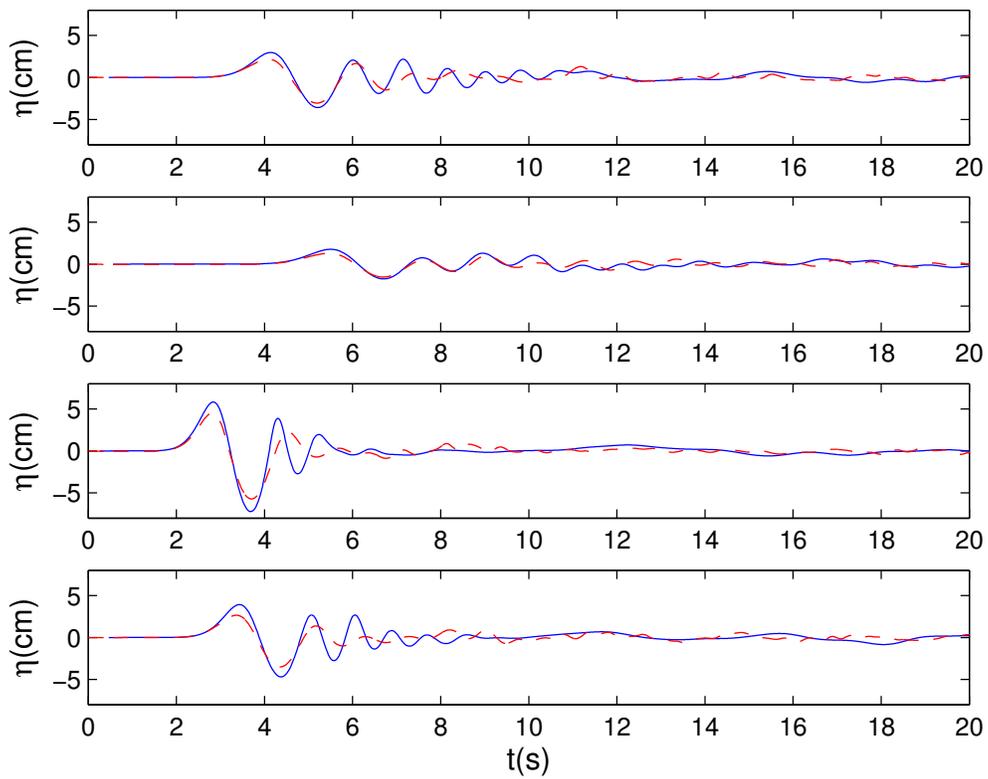
Figure 41: Benchmark 6: Model-data comparisons of tsunami waves for stations 17 to 20.

3.7 Benchmark 7: Slide at Port Valdez, AK during 1964 Alaska Earthquake

Benchmark 7 is based on the historical submarine landslide event happening in Port Valdez, AK during the 1964 Alaska earthquake. The viscous slide model described in Section 2.3 is employed in this case to simulate the fluid-like motion of the slide. The earthquake triggered two main landslides of which one happens at the head of Port Valdez (HPV slide) with slide volume of about 55 million m^3 and another happens at the Shoup Bay moraine (SBM slide) with volume of about 255 million m^3 (Nicolsky et al., 2013). Figure 42 shows the schematic view of Port Valdez with location and thickness of two slides. The slide density is assumed to be 2000 kg/m^3 based on the subsurface geotechnical investigation of material near the site conducted by Shannon and Hilts (1973), and the kinematic viscosity of the slide is set to be 0.1 m/s^2. A sensitivity study by Rabinovich et al. (2003) demonstrate the effect of this viscosity on the generated tsunami height is not significant. The Manning friction coefficient is simply set to zero. The only bottom friction is from viscosity with prescribed vertical profile of velocity.

The total simulation time of the case is 800 s. A uniform grid size of 13.2689 m (8/9 arc-seconds) in x-direction (longitude) and 16.4735 m (8/15 arc-seconds) in y-direction (latitude) is used to discretize the computation domain of Port Valdez in 2316×570 cells. Three vertical layers are evenly distributed. Since the slides move offshore on steep slopes, the vertical water velocity is not negligible and therefore the non-hydrostatic pressure is taken into account in this case. It should be noted that such the steepness also ruins the long-wave approximation in current landslide model and brings a certain extent of error. Further studies will be done to overcome this problem. At the open boundary near Valdez Arm, an extra computation domain of 823.672 m width is attached to the main domain as a sponge layer to damp the outgoing waves.

At the beginning of the simulation, we assume the HPV and SMB slides are initially at rest and goes downslope simultaneously. Figure 43 and 44 shows the motion of HPV and SBM slides respectively in three-dimensionally views. Right after their moving, slide sediments accumulate at the middle of the slide since the upper part of the rupture surface is steeper than its lower part. Then, the slide toe speeds up and the lateral spread-out dominates the slide motion. Finally, both slides become very thin and cover an significantly increased surface area on the seafloor.

The generated waves by the slide motion show in Figure 45 and 46. The initial motion of the slides first cause withdrawal of the water offshore, which is seen clearly in the first plot of 20 s, and later the water level surges upward, hits the Cliff Mine and floods the old town. After about 80 s, the front wave generated by the SBM slide starts hitting the Anderson Bay and getting reflected. The wave eastward encounters the front wave generated by the HPV slide at about 155 s, and then the waves start to overlap and cannot be easily distinguished.

Wave elevation at fou locations are measured, which are shown in Figure 42. Three locations are Point 37, Point 38 and Valdez Hotel (see position in Figure 48) in the old town which are flooded during the event, while another is Valdez Narrows navigation light which is overtopped and destroyed. Figure 47 shows the time series of the modeled water wave height at these locations. At Valdez Hotel, the first wave about 0.4 m is generated by the HPV slide and reaches the hotel about 4 minutes after the event, which meets the eyewitness report. Recall the witness reported a

49
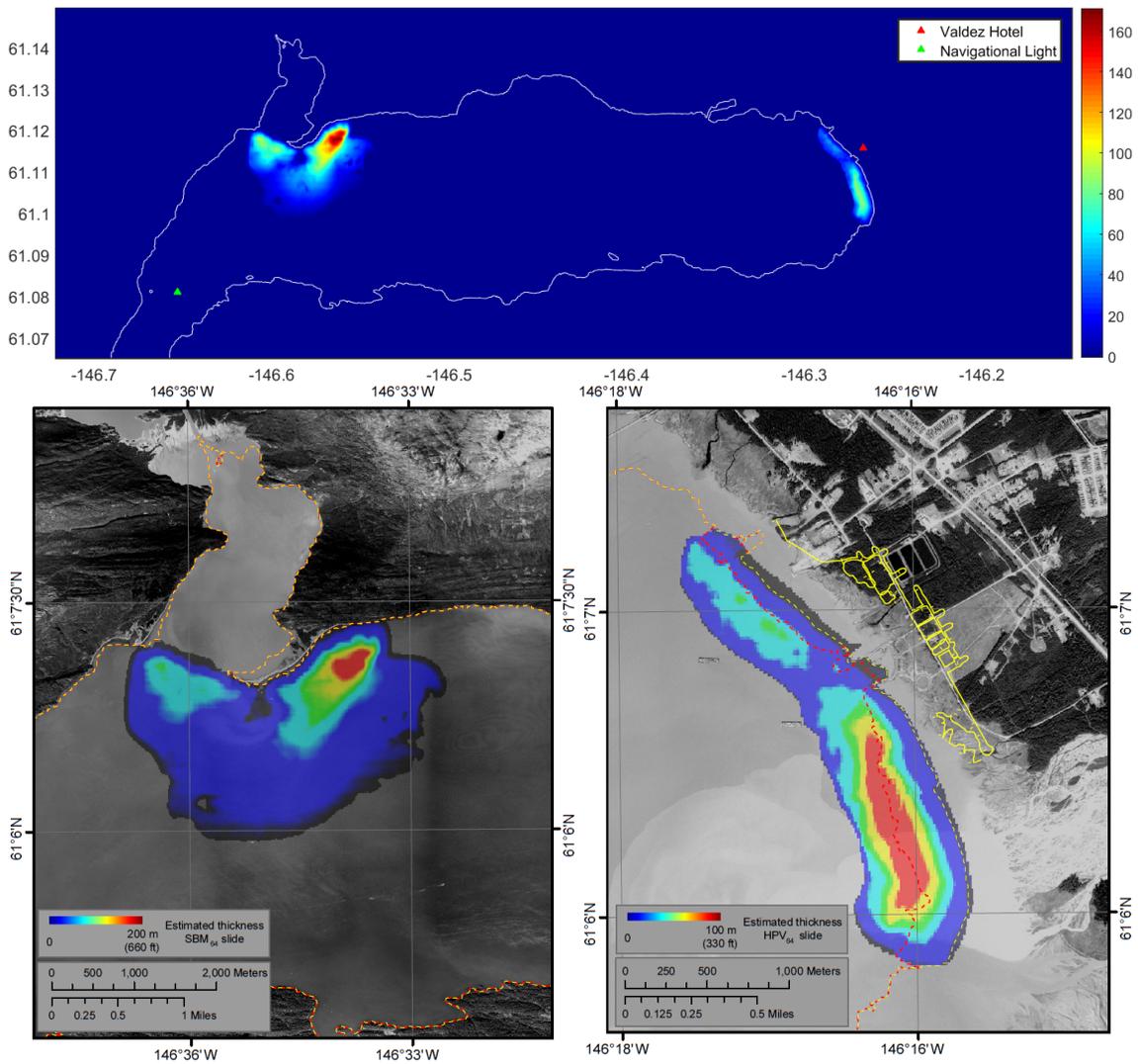
Figure 42: Upper panel: schematic view of Port Valdez with location the two slides; Lower panel: thickness of SBM slide (left) and HPV slide (right). (From Nicolsky et al., 2013)
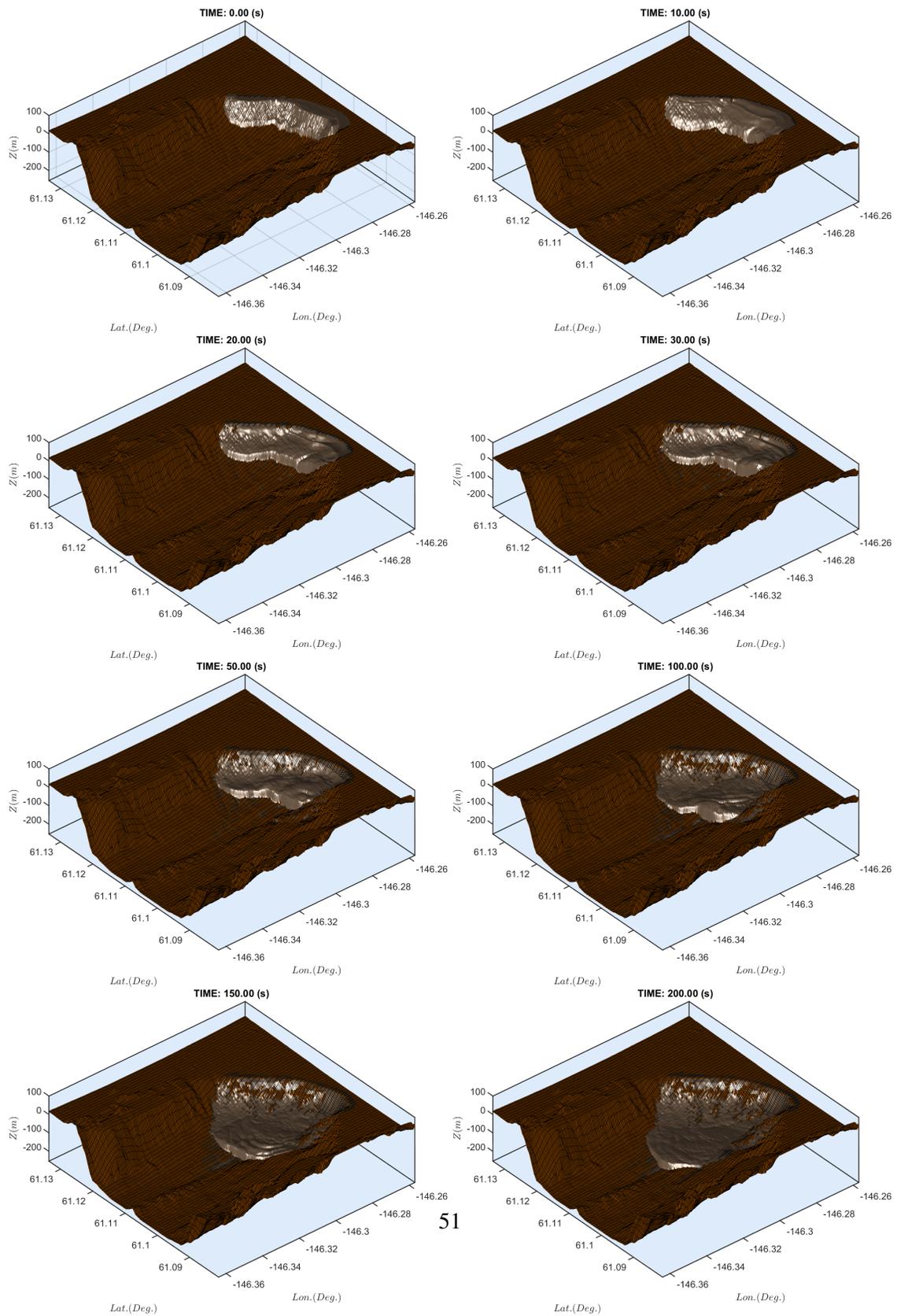
Figure 43: Motion of HPV slide at 0, 10, 20, 30, 50, 100, 150 and 200 s.

51
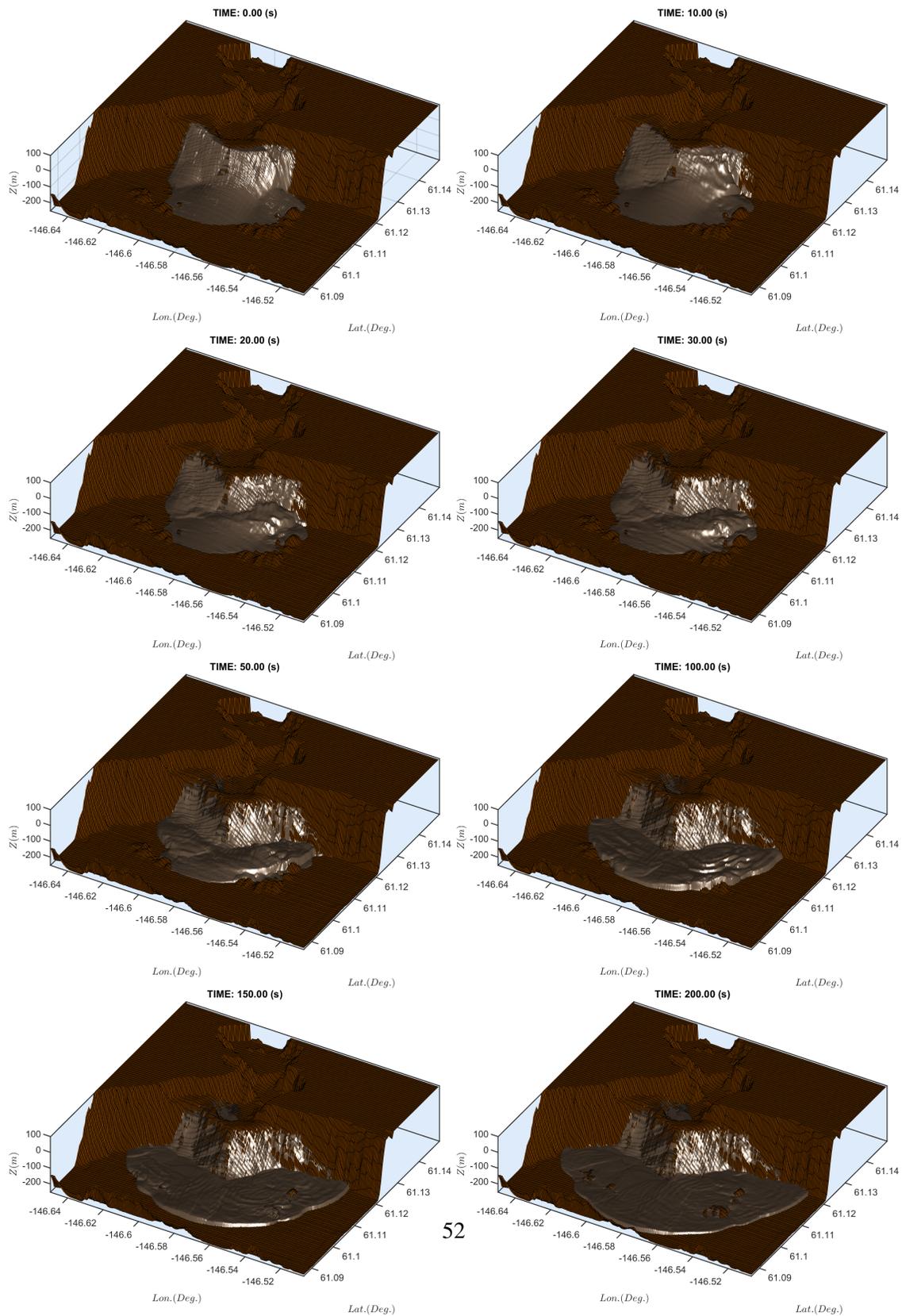
Figure 44: Motion of SBM slide at 0, 10, 20, 30, 50, 100, 150 and 200 s.

52

TIME: 20.00 (s)

TIME: 50.00 (s)

TIME: 80.00 (s)

53
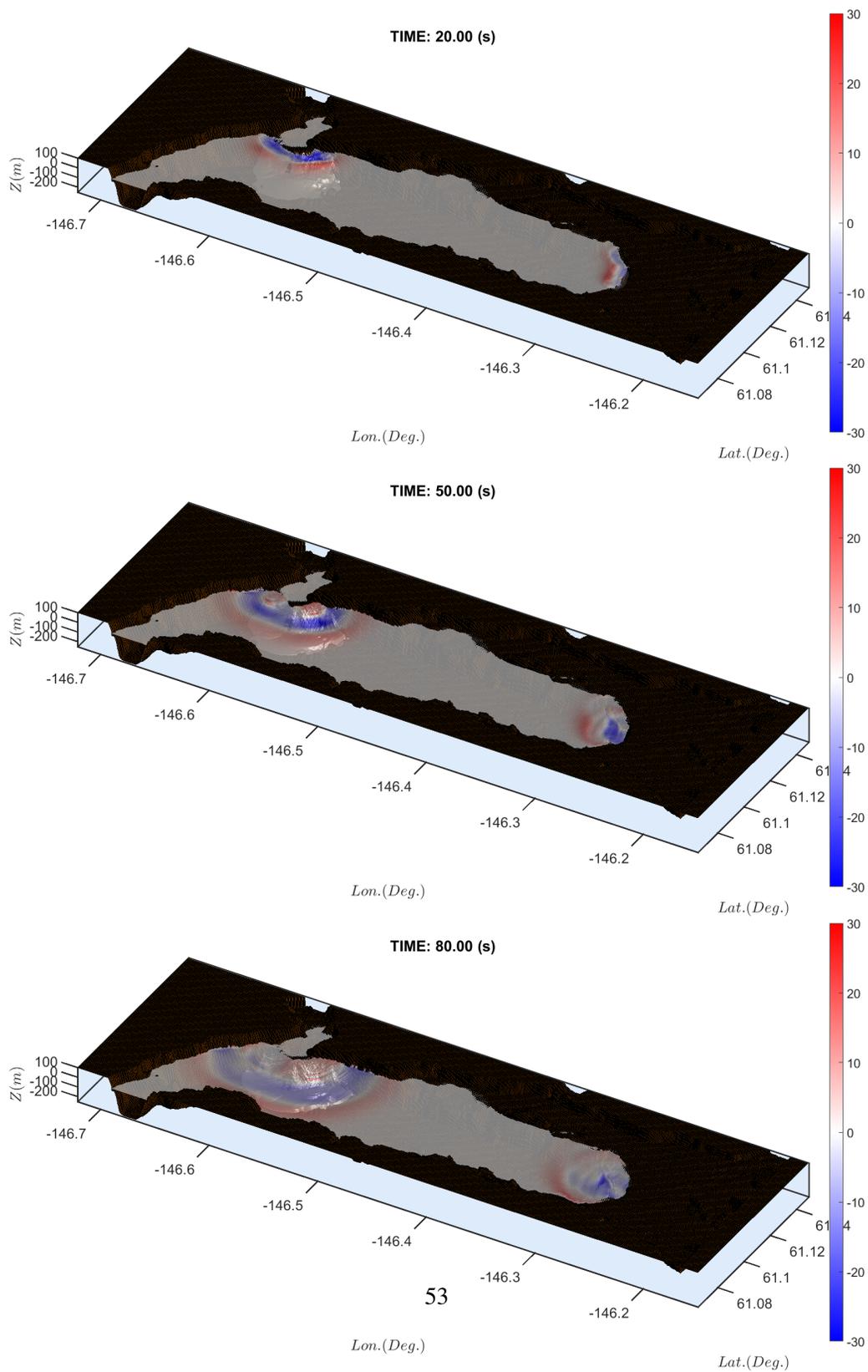
Figure 45: Wave elevation in Port Valdez at 20, 50 and 80 s.

TIME: 155.00 (s)

TIME: 200.00 (s)

TIME: 300.00 (s)

54
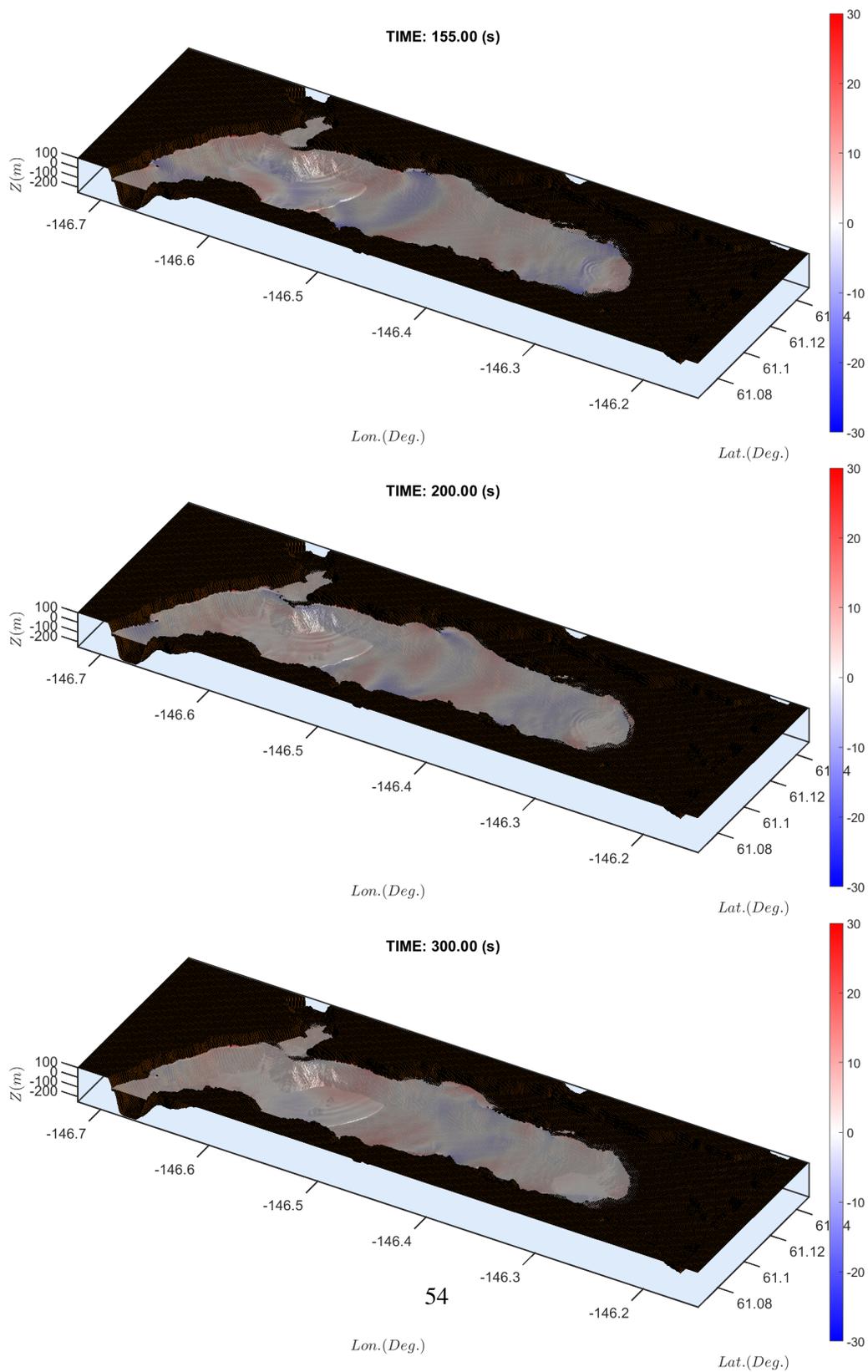
Figure 46: Wave elevation in Port Valdez at 155, 200 and 300 s.

second wave crossed waterfront about 10 minutes after the first one and was a little smaller than the first wave. We observe the second wave from the numerical experiment about 7 minutes after the first one but it is up to about $1.5\ m$ high. We believe the second wave is originated from the SBM slide, and the time and wave height difference is due to the the doubtale assumption that two slides occurs simultaneously. It is possible the initiation of the SBM slide was delayed by $3 - 5$ minutes after the HPV slide (Nicolsky et al., 2013). The maximum runup at the navigation light is about $8\ m$, and the waves are high enough to complete destroy the light that stands on a concrete pylon about $8\ m$ above mean sea level.
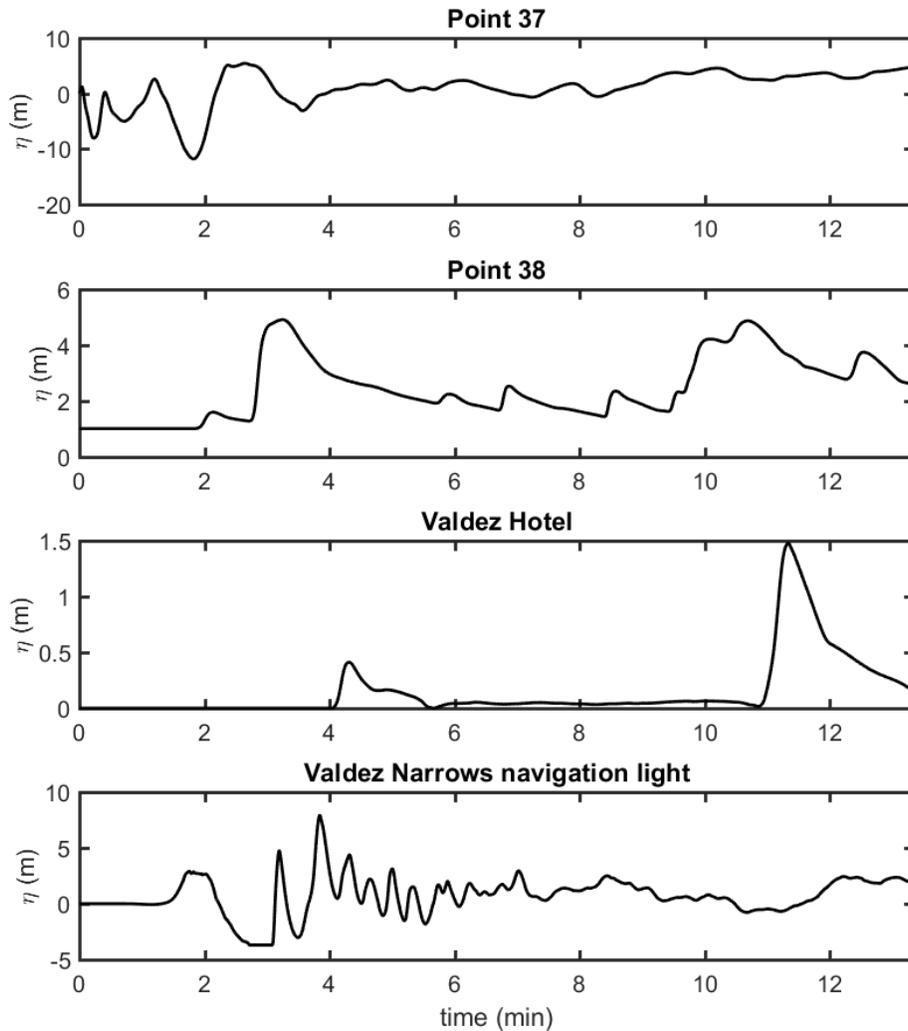
Figure 47: Benchmark 7: Time series of the modeled water wave height at Valdez Hotel (upper panel) and Valdez Narrows navigation light (lower panel).

Figure 48 shows the inundation line at the old town after the first water wave due to the failure of HPV slide. The line covers the observed extent of inundation well. Figure 49 shows the comparison of maximum runup between computation and observation in Port Valdez and Table **??** lists the locations and wave height shown in the figure. Generally, the modeled maximum runup at the locations are a little higher than the observed runup, while at the Cliff Mine and near Valdez Arms the modeled results underestimate the wave height. Nicolsky et al. (2013) encountered the similar problem and they explained the difference by inaccuracies in the assumed SBM slide configuration.

Figure 48: Inundation map at the old town after the first wave.
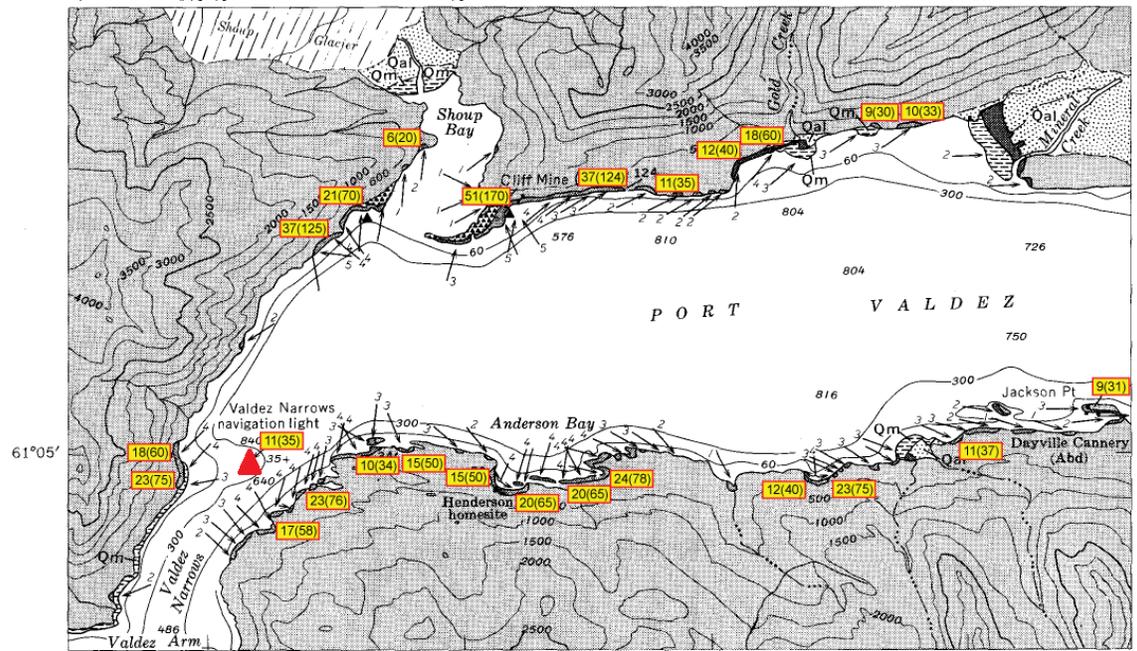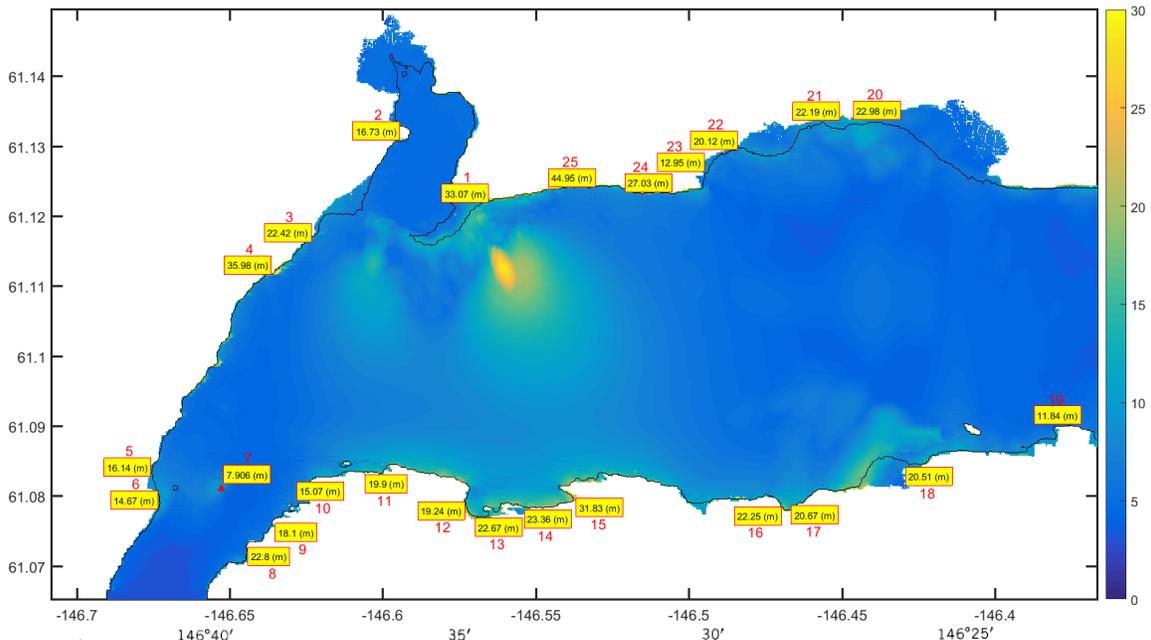
Figure 49: Comparison of maximum runup between computation and observation in Port Valdez..

No.	Location		Max Runup (m)		No.	Location		Max Runup (m)	
	Lon. (deg)	Lat. (deg)	Observed	Modeled		Lon. (deg)	Lat. (deg)	Observed	Modeled
1	-146.5663	61.1224	51	33.0727	14	-146.5428	61.0789	20	23.3635
2	-146.5947	61.1309	6	16.7290	15	-146.5367	61.0793	24	31.8266
3	-146.6236	61.1168	21	22.4235	16	-146.4695	61.0781	12	22.2471
4	-146.6357	61.1118	37	35.9782	17	-146.4594	61.0805	23	20.6692
5	-146.5759	61.0833	18	16.1403	18	-146.4216	61.0850	11	20.5072
6	-146.6732	61.0786	23	14.6696	19	-146.3796	61.0888	9	11.8437
7	-146.6530	61.0811	11	7.9059	20	-146.4453	61.1340	10	22.9762
8	-146.6443	61.0724	17	22.8045	21	-146.4584	61.1339	9	22.1879
9	-146.5354	61.0758	23	18.1019	22	-146.4851	61.1300	18	20.1175
10	-146.6144	61.0829	10	15.0736	23	-146.4959	61.1266	12	12.9498
11	-146.5989	61.0839	15	19.9035	24	-146.5132	61.1232	11	27.0298
12	-146.5727	61.0777	15	19.2445	25	-146.5382	61.1244	27	44.9534
13	-146.5611	61.0783	20	22.6748					

Table 4: Maximum runup at different locations.

4 Conclusions

NHWAVE has been tested against all seven of the proposed benchmarks for the NTHMP landslide tsunami benchmark workshop. The model has been tested in a range of configurations, including solid slide motion (Ma et al., 2012), viscous slide layer motion (Kirby et al., 2016), granular slide motion (Ma et al., 2015), and a 3D suspended load configuration (Ma et al., 2013). Model performance in comparison to data is good, with the major limitation being uncertainty over slide configuration and material properties for the field case in Benchmark 7.

References

Enet F. and Grilli S.T., 2007, "Experimental study of tsunami generation by three-dimensional rigid underwater landslides", *J. Waterway, Port, Coast. Ocean Engrng.*, **133**, 442-454.

Fine, I., Rabinovich A., Kulikov E., Thomson R. and Bornhold B., 1998, "Numerical modelling of landslide-generated tsunamis with application to the Skagway Harbor tsunami of November 3, 1994", *Proc.International Conference on Tsunamis, Paris*, 211-223.

Gottlieb, S., Shu C.-W., and Tadmore, E., 2001, "Strong stability-preserving high-order time discretization methods", *SIAM Review*, **43** (1), 89 - 112.

Grilli, S.T. and Watts, P., 2005, "Tsunami generation by submarine mass failure. I: Modeling, experimental validation, and sensitivity analyses", *J. Waterway, Port, Coast. Ocean Engnrng*, **131**(6), 283-297.

Grilli, S.T., Shelby, M., Kimmoun, O., Dupont, G., Nicolsky, D., Ma, G., Kirby J.T. and Shi F., 2016, "Modeling coastal tsunami hazard from submarine mass failures: effect of slide rheology, experimental validation, and case studies off the US East Coast", *Natural Hazards*, **86**(1), 353-391.

Iverson, R. M. and Denlinger, R. P., 2001, "Flow of variably fluidized granular masses across three-dimensional terrain 1. Coulomb mixture theory", *Journal of Geophysical Research*, **106**, 537-552

Jiang, L. and LeBlond, P. H., 1992, "The coupling of a submarine slide and the surface waves which it generates", *Journal of Geophysical Research: Oceans*, **97**(C8), 12731-12744.

Kirby, J. T., Shi, F., Nicolsky, D. and Misra, S., 2016, "The 27 April 1975 Kitimat, British Columbia submarine landslide tsunami: A comparison of modeling approaches", *Landslides*, **13**, 1421-1434, doi:10.1007/s10346-016-0682-x.

Liu, P.F., Wu, T.R., Raichlen, F., Synolakis, C.E. and Borrero, J.C., 2005, "Runup and rundown generated by three-dimensional sliding masses", *Journal of Fluid Mechanics*, **536**, 107-144.

Ma, G., Shi F. and Kirby J.T., 2012, "Shock-capturing non-hydrostatic model for fully dispersive surface wave processes", *Ocean Modelling*, **43**, 22-35.

Ma, G., Kirby, J. T. and Shi, F., 2013, "Numerical simulation of tsunami waves generated by deformable submarine landslides", *Ocean Modelling*, **69**, 146-165, doi:10.1016/ j.ocemod.2013.07.001.

Ma G., Kirby J.T., Hsu T.-J. and Shi F., 2015, "A two-layer granular landslide model for tsunami wave generation: Theory and computation", *Ocean Modelling*, **93**, 40-55, doi:10.1016/ j.ocemod.2015.07.012.

Mohammed F. and Fritz H.M., (2012), "Physical modeling of tsunamis generated by three-dimensional deformable granular landslides", *J. geophys. Res.*, **117**, C11

Nicolsky, D.J., Suleimani, E.N., Haeussler, P.J., Ryan, H.F., Koehler, R.D., Combellick, R.A. and Hansen, R.A., 2013, "Tsunami inundation maps of Port Valdez, Alaska", *Alaska Division of Geological & Geophysical Surveys Report of Investigation 2013-1*, 1-77

Rabinovich, A. B., Thomson, R. E., Bornhold, B. D., Fine, I. V. and Kulikov, E. A., 2003, "Numerical modelling of tsunamis generated by hypothetical landslides in the Strait of Georgia, British Columbia", *Pure and Applied Geophysics*, **160**(7), 1273-1313.

Shannon, W., and Hilts, D., 1973, "Submarine landslide at Seward, in The Great Alaska Earthquake of 1964" *Washington, DC, ??Engineering ??(National Academy of Sciences)*, 144-156.

Wu, T. R., 2004, "A numerical study of three-dimensional breaking waves and turbulence effects", PhD. Dissertation, Cornell University.